1. Introduction

Discrete approximation of horizontal pressure-gradient force (PGF) topography-following coordinates has been a long-standing problem in atmospheric and oceanic modeling (Gary, 1973; Mesinger & Arakawa, 1976; Janjic, 1977; Mesinger, 1982; Arakawa & Suarez, 1983; Mesinger & Janjic, 1985; Michailovich & Janjic, 1986; Blumberg & Mellor, 1987; Haney, 1991; Mellor *et al*, 1994; Stelling & van Kester, 1994; Song & Haidvogel, 1994; Lin, 1997, 1998; Slordal, 1997; Janjic, T., 1998; Mellor *et al*, 1998; Song, 1998; Song & Wright, 1998; Kliem & Pietrzak, 1999). The main difficulty is attributed to *hydrostatic inconsistency*, i.e., failure of the discretized PGF to vanish in the case when isopycnals are horizontal. This effect causes spurious geostrophically balanced flows, which in oceanic model applications may be as large as 10 cm/s or more, degrading the quality of the solution beyond an acceptable limit. The problem arises from the deviation of quasi-horizontal coordinates from either geopotential or isopycnal surfaces, so that the PGF in the momentum equations appears in the form of two large terms which tend to cancel each other,

$$-\frac{1}{\rho_0}\frac{\partial P}{\partial x}\bigg|_z = -\frac{1}{\rho_0}\frac{\partial P}{\partial x}\bigg|_s + \frac{1}{\rho_0}\cdot\frac{\partial P}{\partial z}\cdot\frac{\partial z}{\partial x}\bigg|_s \,, \tag{1.1}$$

where P is pressure, $\rho_0 = $ const is mean density in a Boussinesq approximation, and z is vertical coordinate in non-transformed (i.e., physical) space. Subscript z in $\partial/\partial x|_z$ means that the associated partial derivative is computed with respect to a constant geopotential surface, $z = $ const, and a similar subscript s means that the differentiation is performed along the transformed coordinate surface, $s = $ const.

In the present study we are not limited to the traditional σ-coordinate,

$$z(x,y,\sigma) = h(x,y)\cdot f(\sigma)\,, \qquad -1 \le \sigma \le 0\,, \tag{1.2}$$

where $h(x,y)$ is oceanic bottom depth, and $f(\sigma)$ is a monotonic mapping function independent of horizontal coordinates that controls vertical-coordinate (hence grid) stretching. Instead we assume that the three-dimensional mapping function $z = Z(x,y,s,t)$ is both monotonic (i.e., $\partial Z \big/ \partial s > 0$) and nonseparable, while usually

$$\frac{\partial Z}{\partial x}\bigg|_s \ne 0\,. \tag{1.3}$$

Moreover, it is assumed that (1.1) may be stiff in the sense that

$$\epsilon \equiv \frac{\left|\frac{\partial P}{\partial x}\big|_s - \frac{\partial P}{\partial z}\cdot\frac{\partial z}{\partial x}\big|_s\right|}{\left|\frac{\partial P}{\partial x}\big|_s\right| + \left|\frac{\partial P}{\partial z}\cdot\frac{\partial z}{\partial x}\big|_s\right|} \ll 1\,, \tag{1.4}$$

which indicates that special precautions need to be taken to avoid loss of accuracy [1].

P is computed from the hydrostatic equation,

$$P(x,y,z) = g\int_z^{\zeta} \rho(x,y,z')\mathrm{d}z'\,, \tag{1.5}$$

where $\rho(x,y,z)$ is density; ζ is free-surface elevation; and g is gravitational acceleration. One might be tempted to replace (1.1) with

$$-\frac{1}{\rho_0}\frac{\partial P}{\partial x}\bigg|_z = -\frac{1}{\rho_0}\frac{\partial P}{\partial x}\bigg|_s - \frac{g\rho}{\rho_0}\cdot\frac{\partial z}{\partial x}\bigg|_s \,, \tag{1.6}$$

and discretize it in a straightforward way using second-order averaging and differencing operators. This was shown to be prone to hydrostatic consistency error (cf., Mesinger & Arakawa, 1976), caused mainly by the vertical averaging of P and horizontal averaging of ρ in (1.6) in order to co-locate them with horizontal velocity components on a staggered grid.

Practical experience has resulted in essentially two approaches to overcome this problem:

(i) In each vertical column compute a set of values of pressure $P_{k+\frac{1}{2}}$ naturally located half-way between the density points on a staggered vertical grid; then for each two neighboring columns, interpolate this P field to an appropriate common geopotential level; and then subtract the interpolated values. Note, that after computation of P, the density field ρ_k does not participate in any further computation. Obviously, in this approach the two terms in (1.1) become inseparable. The different methods of this family may vary in details of the choice of the common level as well as interpolation technique, which is linear in most cases (Janjic, 1977; Arakawa & Suarez, 1983; Lin, 1997) or parabolic (Michailovich & Janjic, 1986). Overall, the overwhelming majority of atmospheric models use schemes belonging to this class.

(ii) Following Blumberg & Mellor, 1987, and Song, 1998, Eqs. (1.1)—(1.5) are first transformed into

$$-\frac{1}{\rho_0}\frac{\partial P}{\partial x}\bigg|_z = -\frac{1}{\rho_0}\frac{\partial P}{\partial x}\bigg|_{z=\zeta} - \frac{g}{\rho_0}\int_z^{\zeta}\frac{\partial \rho}{\partial x}\bigg|_z \mathrm{d}z' \tag{1.7}$$

$$= -\frac{g\rho(\zeta)}{\rho_0}\frac{\partial\zeta}{\partial x} - \frac{g}{\rho_0}\int_z^{\zeta}\left[\frac{\partial\rho}{\partial x}\bigg|_s - \frac{\partial\rho}{\partial z'}\,\frac{\partial z'}{\partial x}\bigg|_s\right]\mathrm{d}z'\,,$$

[1] We will use the terminology of σ-coordinate and σ-modeling throughout this paper in a broad sense referring to the whole class of models with a non-aligned vertical coordinate

tinuous expression for the PGF,

$$-\left.\frac{\partial P}{\partial x}\right|_z = -\rho_s g \frac{\partial \zeta}{\partial x} - g \int_z^{\zeta} \mathcal{J}(\rho, z) ds\,, \tag{2.1}$$

where

$$\mathcal{J}(\rho, z) = \left.\frac{\partial \rho}{\partial x}\right|_s \frac{\partial z}{\partial s} - \frac{\partial \rho}{\partial s} \left.\frac{\partial z}{\partial x}\right|_s\,, \tag{2.2}$$

ζ is free-surface elevation, ρ_s is density at the surface, and g is acceleration of gravity. POM/SCRUM use the most straightforward second-order accuracy method to approximate (2.2) [3],

$$\begin{aligned} -\Delta x \Delta s\ \mathcal{J}(\rho, z) = \frac{1}{4} & \left[(\rho_1 + \rho_2 - \rho_3 - \rho_4) \right. \\ & \times (z_2 - z_1 + z_4 - z_3) \\ & - (\rho_2 - \rho_1 + \rho_4 - \rho_3) \\ & \left. \times (z_1 + z_2 - z_3 - z_4) \right]\,, \end{aligned} \tag{2.3}$$

where placement of values with indices 1,2,3,4 is shown on Fig. 1. Since (2.3) treats ρ and z in a symmetric way, it has the property of antisymmetry,

$$\mathcal{J}(\rho, z) = -\mathcal{J}(z, \rho)\,, \tag{2.4}$$

and, obviously, it vanishes identically if ρ is a linear function of z.

This discretization can be rewritten in four algebraically equivalent forms **(i)**–**(iv)**:

(i) "Diagonal" Jacobian:

$$\begin{aligned} -\Delta x \Delta s\ \mathcal{J}(\rho, z) = \frac{1}{2} & \left[(\rho_2 - \rho_3)(z_4 - z_1) \right. \\ & \left. + (\rho_1 - \rho_4)(z_2 - z_3) \right]\,, \end{aligned} \tag{2.5}$$

(ii) Horizontal (along-geopotential) differencing of ρ linearly interpolated or extrapolated within each vertical column to a common level z_*:

$$-\Delta x \Delta s\ \mathcal{J}(\rho, z) = \mathcal{A}\left(\rho_*^L - \rho_*^R\right)\,, \tag{2.6}$$

where

$$\mathcal{A} = \Delta x \frac{z_2 - z_1 + z_4 - z_3}{2} \tag{2.7}$$

is the area of trapezoidal element (z_1, z_3, z_4, z_2),

$$\begin{aligned} \rho_*^L &= \frac{\rho_1 (z_2 - z_*) + \rho_2 (z_* - z_1)}{z_2 - z_1} \\ \rho_*^R &= \frac{\rho_3 (z_4 - z_*) + \rho_4 (z_* - z_3)}{z_4 - z_3}\,, \end{aligned}$$

[3] Here we follow notation of Song, 1998. Eq. (5) from Mellor *et al*, 1994 becomes equivalent to (2.3) after it is recognized that $z_{i,k} = H_i \sigma_k$ in their notation.

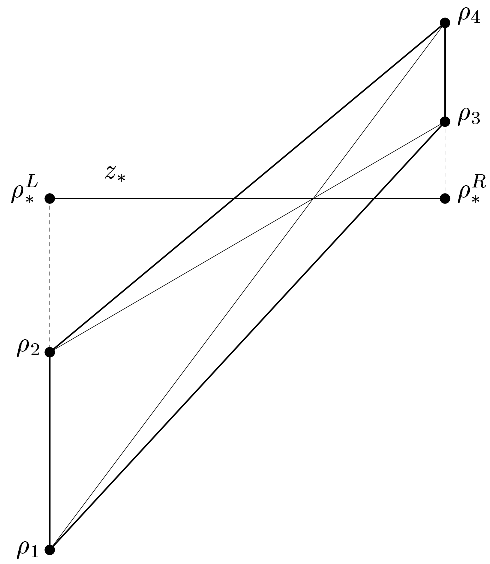

Figure 1. An elementary computational stencil of POM density Jacobian.

and

$$z_* = \frac{z_4 z_2 - z_3 z_1}{z_4 - z_3 + z_2 - z_1}\,, \tag{2.8}$$

which coincides with the level of intersection of diagonals of trapezoidal element (Fig. 1). This choice of z_* also has the property,

$$\frac{z_* - \frac{1}{2}(z_1 + z_2)}{z_2 - z_1} = \frac{\frac{1}{2}(z_3 + z_4) - z_*}{z_4 - z_3}\,, \tag{2.9}$$

which implies that offsets from mid-level to z_* are proportional to grid-box height in each vertical column of ρ locations. The possibility to rewrite (2.3) into (2.6)–(2.8) indicates that, unlike stated in Mellor *et al*, 1994, 1998, and Song, 1998, Jacobian formulation by itself does not offer any relief from violation of hydrostatic consistency condition (Haney, 1991) when

$$r_x = \frac{z_4 + z_3 - z_2 - z_1}{z_4 - z_3 + z_2 - z_1} > 1 \tag{2.10}$$

becomes greater than one and vertical interpolation of ρ turns into extrapolation. However, this choice of z_* delays this moment as much as possible among all possible schemes using the stencil shown on Fig. 1, since proportionality (2.9) makes the transition from interpolation to extrapolation occur at the same time for both left and right vertical columns at ρ locations. (Any choice of z_* other than (2.8) would cause the transition to occur earlier at one end.) Note that violation of the hydrostatic consistency criterion (2.10) does not mean immediate hydrostatic instability because after vertical integration of larly, PGF at the topmost grid box cannot be computed via regular Jacobian scheme because this would require values of ρ above or at the surface that are not available). POM/SCRUM simply use the nearest available value $\rho_{i,N}$,

$$P_{i,N} = g\rho_{i,N}\left(\zeta_i - z_{i,N}\right)\,, \tag{2.17}$$

which is equivalent to the assumption that ρ is vertically uniform within the topmost grid box. In terms of the resultant PGF at the topmost grid box, this assumption neglects the hydrostatic compensation term, effectively neglecting the σ-coordinate slope within the topmost grid box. A more accurate treatment of the topmost grid box is given by (A.21) in Appendix A.

Representation of (2.3) in pseudo-flux form (2.11)–(2.12) and in σ-coordinate primitive form opens the possibility to proof that a model which uses this PGF discretization and a second-order centered advection scheme for the density equation is energetically consistent in the sense that it conserves exactly the sum of discrete kinetic and potential energy (Song & Wright, 1998). This property is often invoked as useful for long-term stability of integration. The practical usefulness of this property, as well as the possibility to extend its proof to higher orders of accuracy, will is discussed later.

3. Weighted Jacobian of Song (1998)

Song (1998) proposes replacing equal-weight vertical averages in (2.3) with weighting according to

$$\begin{aligned} -\Delta x\Delta s\;\mathcal{J}(\rho,z) = \frac{1}{2}\,&\big[(\alpha\rho_1+\beta\rho_2-\alpha\rho_3-\beta\rho_4) \\ &\times(z_2-z_1+z_4-z_3) \\ &-(\rho_2-\rho_1+\rho_4-\rho_3) \\ &\times(\alpha z_1+\beta z_2-\alpha z_3-\beta z_4)\big]\,, \end{aligned} \tag{3.1}$$

where α and $\beta \equiv 1-\alpha$ are chosen from the condition that the scheme is able to produce exact dynamic PGF at the location

$$z_C = \frac{z_1+z_2+z_3+z_4}{4} \tag{3.2}$$

if ρ is a bi-linear function of x and z. This choice results in $\alpha = \frac{1}{2}-\epsilon$, $\beta = \frac{1}{2}+\epsilon$, where

$$\epsilon = \frac{(z_4+z_3-z_2-z_1)\,(z_4-z_3-z_2+z_1)}{8\,(z_4-z_3)\,(z_2-z_1)}\,, \tag{3.3}$$

which is (2.15) from Song, 1998, rewritten in our notation.

The weighting (3.1) destroys the antisymmetry property (2.4) of the original Jacobian, as well as the possibility to rewrite it into diagonal, pseudo-flux, and *sigma*-coordinate primitive forms. Hence, it is no longer possible to prove energetic consistency in a manner similar to Song & Wright, 1998. Also lost is the property of hydrostatic error cancellation when $z_2 = z_3$ or $z_1 = z_4$. However, the property of zero error if ρ is linear function of z is maintained. Examination of (3.3) reveals that the scheme is equivalent to (2.6)–(2.8), when z_* is replaced with z_C, the derivation of which is evident from Fig. 3.

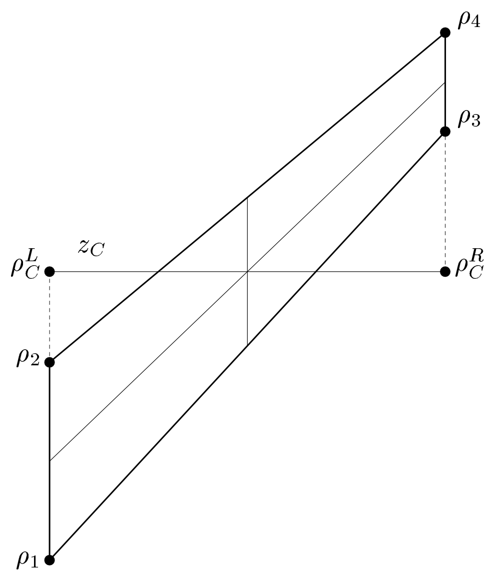

Figure 3. Explanation of Weighted Jacobian of Song (1998): at each side density is interpolated or extrapolated linearly toward common level z_C, which is chosen to be at the midlevel, after which the interpolated values are differenced horizontally.

In retrospect one can conclude that the original equally-weighted Jacobian evaluates the horizontal (along-geopotential) ρ gradient exactly at level z_*, which is the level of intersection of diagonals, if ρ is a bi-linear function of x and z. Therefore, contrary to the claim of Song, 1998, weighted Jacobian does not offer any theoretical advantage over the standard Jacobian in the case where a more general ρ perturbation is present; instead, these two schemes correspond to just two *ad hoc* choices for the common level z_* (or z_C) to which ρ is interpolated before horizontal differencing, and they both are exact in special cases described above.

4. Sensitivity to Choice of z_*: Seamount Test Problem

One might guess that the difference between standard and weighted Jacobians is minor, because it is nothing more than a particular choice of the common level z_*, and

The initial ρ profile is defined by

$$\rho(z) = 3e^{z/\delta}\,, \quad -h(x,y) \le z \le 0\,, \tag{4.7}$$

where, as in the more oceanographically realistic study of Beckmann & Haidvogel, 1997, we chose $\delta = 500\,m$ which results in twice as steeper stratification of ρ in comparison with previous idealized studies cited above. Eq. (4.7) results in a Burger number,

$$S = \frac{\sqrt{gh\cdot\Delta\rho/\rho}}{fL} \approx \frac{\left(9.81\cdot 5\times 10^3\cdot 3/10^3\right)^{1/2}}{10^{-4}\cdot 40\times 10^3} \approx 3.1\,, \tag{4.8}$$

which is a typical midrange value among those used in Beckmann & Haidvogel, 1993, Mellor *et al*, 1998.

A horizontal Laplacian viscosity is set to $50\,m^2/s$ in all calculations presented here. This value is chosen to be comparable with that used in realistic simulations at similar resolution, and it is 40 times smaller that reported in Mellor *et al*, 1998, and 10 times smaller than in Song, 1998. Vertical viscosity, and horizontal and vertical diffusivities for tracers are all set to zero.

Tracer advection (here for ρ) is discretized using monotonized, fourth-order, centered scheme, i.e., in order to compute advective flux at the velocity component location $u_{i+\frac{1}{2},j,k}$, we use an interpolation scheme,

$$\rho_{i+\frac{1}{2},j,k} = \frac{\rho_{i,j,k}+\rho_{i+1,j,k}}{2} - \frac{\delta\rho_{i+1,j,k}-\delta\rho_{i,j,k}}{6}\,, \tag{4.9}$$

where $\delta\rho_{i,j,k}$ is mean slope defined at the location of $\rho_{i,j,k}$ using a harmonic average,

$$\delta\rho_{i,j,k} = \frac{2\Delta\rho_{i+\frac{1}{2},j,k}\Delta\rho_{i-\frac{1}{2},j,k}}{\Delta\rho_{i+\frac{1}{2},j,k}+\Delta\rho_{i-\frac{1}{2},j,k}}\,, \tag{4.10}$$

if $\Delta\rho_{i+\frac{1}{2},j,k}$ and $\Delta\rho_{i-\frac{1}{2},j,k}$ have the same sign and

$$\delta\rho_{i,j,k} = 0\,, \tag{4.11}$$

if the signs are different, and

$$\Delta\rho_{i+\frac{1}{2},j,k} = \rho_{i+1,j,k} - \rho_{i,j,k} \tag{4.12}$$

are elementary differences of ρ. Obviously, if (4.10) is replaced with algebraic mean of $\Delta\rho_{i+\frac{1}{2},j,k}$ and $\Delta\rho_{i-\frac{1}{2},j,k}$, then (4.9) becomes equivalent to a more familiar fourth-order interpolation scheme,

$$\rho_{i+\frac{1}{2},j,k} = \frac{-\rho_{i-1,j,k}+7\rho_{i,j,k}+7\rho_{i+1,j,k}-\rho_{i+2,j,k}}{12}\,. \tag{4.13}$$

The use of (4.10) guarantees that the averaged value of slope never exceeds twice the smaller of the two adjacent elementary differences. It also makes the interpolated value $\rho_{i+\frac{1}{2},j,k}$ be always between $\rho_{i,j,k}$ and $\rho_{i+1,j,k}$ regardless of sharp changes in the slope of the interpolated field (cf., van Leer, 1977). In places where the advected field $\rho_{i,j,k}$ is sufficiently smooth, these consecutive differences are comparable, and the difference between algebraic and harmonic means disappears, making the scheme behave like a fourth-order accurate scheme. In the next section we will discuss the effect of using harmonic averaging in more detail. The ρ advection used here is non-dissipative, since neither explicit diffusion nor an upstream-biased advection scheme is used.

The present setup differs substantially from all similar previous studies in two aspects:

- We do not subtract any background $\rho(z)$ profile when computing PGF; rather the full *in situ* ρ is used.
- Our primary criterion in evaluating the results is not the initial hydrostatic error, but rather long-term behavior of the solution. Therefore we carry out all our test runs to relatively large time of 6 months, which is sufficient to ensure that there is no further error growth (typically the duration of the test runs was 5, 10, 20 and 30 days in the previous studies cited here).

In our seamount experiment we compute time of histories the following quantities:

kinetic energy,

$$\mathcal{E}_{\text{kin}} = \frac{1}{2\mathcal{V}}\sum_{i,j,k}\left[\Delta\mathcal{V}_{i+\frac{1}{2},j,k}u^2_{i+\frac{1}{2},j,k} + \Delta\mathcal{V}_{i,j+\frac{1}{2},k}v^2_{i,j+\frac{1}{2},k}\right]\,, \tag{4.14}$$

barotropic kinetic energy fraction,

$$f_{\text{bar}} = \mathcal{E}_{\text{bar}}/\mathcal{E}_{\text{kin}}\,, \tag{4.15}$$

where $\mathcal{E}_{\text{bar}}$ is barotropic kinetic energy,

$$\mathcal{E}_{\text{bar}} = \frac{1}{2\mathcal{V}}\sum_{i,j}\left[\overline{\Delta\mathcal{V}}_{i+\frac{1}{2},j}\overline{u}^2_{i+\frac{1}{2},j} + \overline{\Delta\mathcal{V}}_{i,j+\frac{1}{2}}\overline{v}^2_{i,j+\frac{1}{2}}\right]\,, \tag{4.16}$$

maximum velocity,

$$V_{\max} = \max\left\{u_{i+\frac{1}{2},j,k}\,,\, v_{i,j+\frac{1}{2},k}\right\} \tag{4.17}$$

maximum barotropic velocity,

$$\langle V\rangle_{\max} = \max\left\{\overline{u}_{i+\frac{1}{2},j}\,,\,\overline{v}_{i,j+\frac{1}{2}}\right\}\,, \tag{4.18}$$

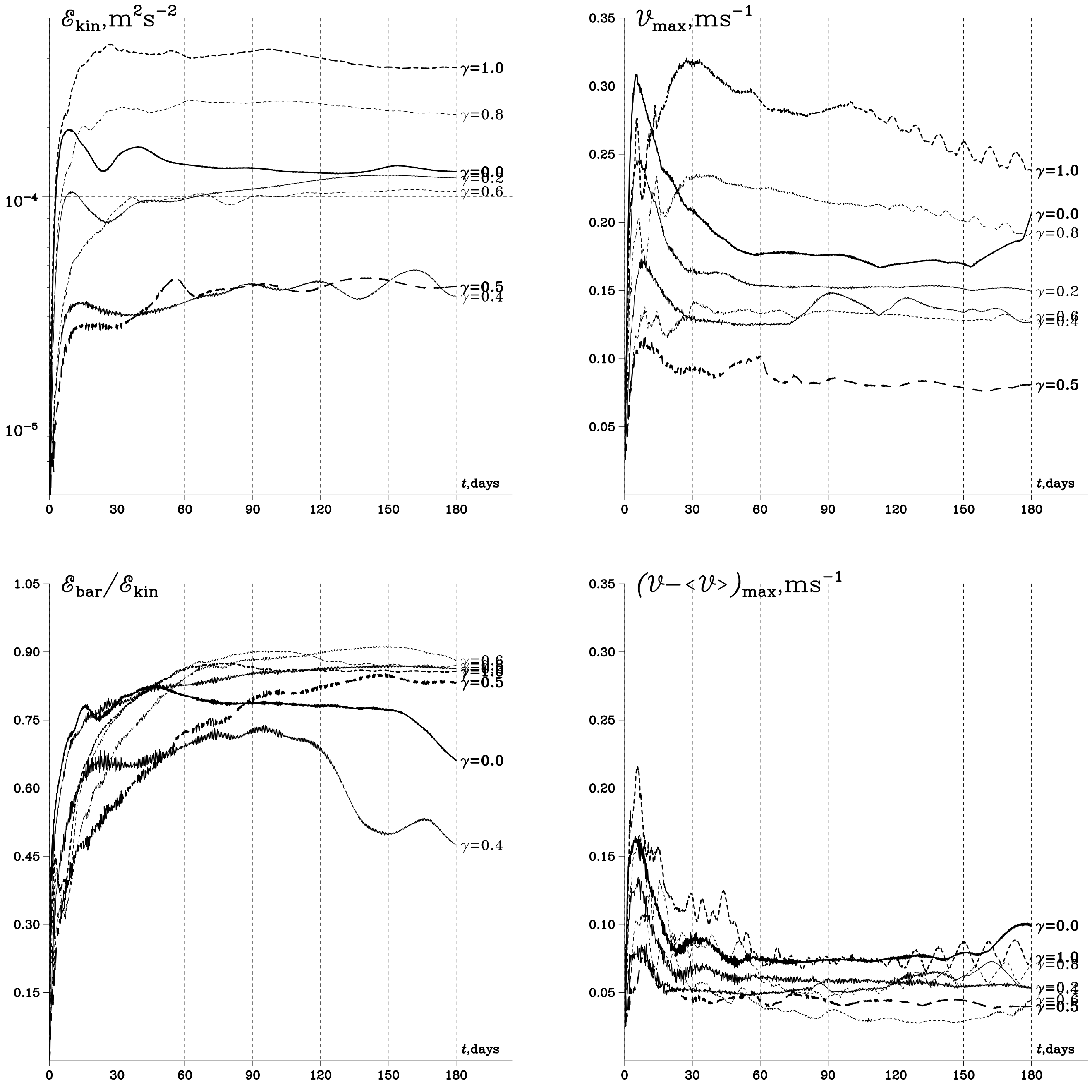

Figure 5. Time histories of net kinetic energy $\mathcal{E}_{\text{kin}}$; fraction of barotropic kinetic energy $\mathcal{E}_{\text{bar}}/\mathcal{E}_{\text{kin}}$; maximum velocity $V_{\max}$; and maximum baroclinic velocity $|V - < V >|_{\max}$ for a coarse-resolution Seamount test problem on a $(48\times48\times11$ grid) for different values of weighting parameter γ. Solid lines are for $0 \le \gamma \le 0.5$, dashed are for $\gamma > 0.5$. Bold lines are for $\gamma = 0$ (POM Jacobian), $\gamma = 1$ (weighted Jacobian of Song, 1998) and $\gamma = 0.5$ ("optimum" weighting). Note that baroclinic velocity error is relatively insensitive to the choice of γ, and after long-term integration the error becomes predominantly barotropic.

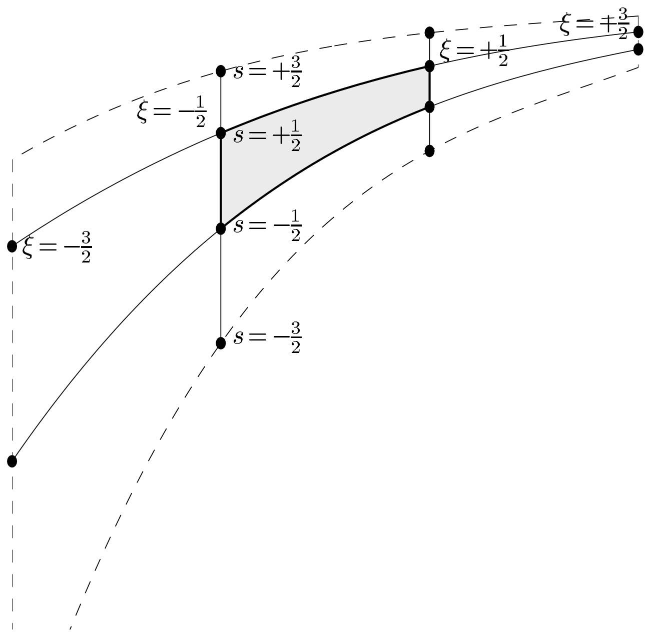

Figure 7. Stencil for pressure-gradient scheme with cubic polynomial fits. Bullets indicate ρ and z points involved in computation of integral of $\left.\frac{\partial\rho}{\partial x}\right|_z$ over shaded area. Because cubic interpolation is used to reconstruct coordinate lines, this appears to be a smooth version of Fig. 1.

The next possibility is to use 4-point cubic Lagrange polynomial fit for ρ, which passes exactly through points $\rho_{i,k-1}$, $\rho_{i,k}$, $\rho_{i,k+1}$, and $\rho_{i,k+2}$ (z is treated similarly), and then integrate analytically between the points $\rho_{i,k}$ and $\rho_{i,k+1}$:

$$f(\xi) = f^{(0)} + f^{(1)}\xi + f^{(2)}\frac{\xi^2}{2} + f^{(3)}\frac{\xi^3}{6}\,, \tag{5.5}$$

where

$$\begin{aligned} f^{(0)} &= \frac{9}{16}\left(f_{\frac{1}{2}} + f_{-\frac{1}{2}}\right) - \frac{1}{16}\left(f_{\frac{3}{2}} + f_{-\frac{3}{2}}\right) \\ f^{(1)} &= \frac{9}{8}\left(f_{\frac{1}{2}} - f_{-\frac{1}{2}}\right) - \frac{1}{24}\left(f_{\frac{3}{2}} - f_{-\frac{3}{2}}\right) \\ f^{(2)} &= \frac{1}{2}\left(f_{\frac{3}{2}} - f_{\frac{1}{2}} - f_{-\frac{1}{2}} + f_{-\frac{3}{2}}\right) \\ f^{(3)} &= f_{\frac{3}{2}} - 3f_{\frac{1}{2}} + 3f_{-\frac{1}{2}} - f_{-\frac{3}{2}}\,. \end{aligned} \tag{5.6}$$

Here we introduce a local fractional coordinate $\xi \in \left(-\frac{1}{2}\,;+\frac{1}{2}\right)$ for the distance between the points. The coefficients (5.6) coincide with fourth-order approximations for mid-point value $f^{(0)}$ and first derivative $f^{(1)}$ and second-order approximations for the second $f^{(2)}$ and third derivatives $f^{(3)}$; this is sufficient to approximate the integral,

$$\int_{-\frac{1}{2}}^{+\frac{1}{2}} f(\xi)\,\mathrm{d}\xi = f^{(0)} - \frac{1}{24}f^{(2)}, \tag{5.7}$$

with fourth order of accuracy. An obvious drawback of this approach is that it is not guaranteed that the right-side limit of the first derivative of the polynomial segment used between points k and $k+1$ matches the left-side limit of segment between $k+1$ and $k+2$ (since these polynomials are obtained from different quartets of points). We therefore abandon the requirement that the cubic polynomial fit pass exactly through extreme points of its stencil, and instead demand that derivatives at $\xi = \pm\frac{1}{2}$ are equal to prescribed values $d_{\pm\frac{1}{2}}$ (whose approximation will be separately specified). This leads to an alternative set of coefficients for (5.5),

$$\begin{aligned} f^{(0)} &= \frac{f_{\frac{1}{2}} + f_{-\frac{1}{2}}}{2} - \frac{d_{\frac{1}{2}} - d_{-\frac{1}{2}}}{8} \\ f^{(1)} &= \frac{3}{2}\left(f_{\frac{1}{2}} - f_{-\frac{1}{2}}\right) - \frac{d_{\frac{1}{2}} + d_{-\frac{1}{2}}}{4} \\ f^{(2)} &= d_{\frac{1}{2}} - d_{-\frac{1}{2}} \\ f^{(3)} &= 6\left(d_{\frac{1}{2}} + d_{-\frac{1}{2}}\right) - 12\left(f_{\frac{1}{2}} - f_{-\frac{1}{2}}\right)\,. \end{aligned} \tag{5.8}$$

It can be verified that (5.5)–(5.8) guarantees that

$$f\left(\pm\frac{1}{2}\right) = f_{k\pm\frac{1}{2}} \qquad \text{and} \qquad \left.\frac{\partial f}{\partial \xi}\right|_{\xi=\pm\frac{1}{2}} = d_{\pm\frac{1}{2}}\,. \tag{5.9}$$

Substitution of polynomial fits (5.5) for both $\rho(\xi)$ and $z(\xi)$ into integrals (5.3)–(5.4) and integration yields

$$\begin{aligned} \int_{-\frac{1}{2}}^{+\frac{1}{2}} \rho\frac{\partial z}{\partial \xi}\mathrm{d}\xi &= \int_{-\frac{1}{2}}^{+\frac{1}{2}} \left[\rho^{(0)} + \rho^{(1)}\xi + \rho^{(2)}\frac{\xi^2}{2}\right. \\ &\quad \left. + \rho^{(3)}\frac{\xi^3}{6}\right]\cdot\left[z^{(1)} + z^{(2)}\xi + z^{(3)}\frac{\xi^2}{2}\right]\mathrm{d}\xi \\ &= \rho^{(0)}z^{(1)} + \frac{1}{24}\rho^{(0)}z^{(3)} + \frac{1}{24}\rho^{(2)}z^{(1)} \\ &\quad + \frac{1}{12}\rho^{(1)}z^{(2)} + \frac{1}{320}\rho^{(2)}z^{(3)} + \frac{1}{480}\rho^{(3)}z^{(2)}\,, \end{aligned} \tag{5.10}$$

which can be used in conjunction with either (5.6) or (5.8).

After substitution of expressions for $\rho^{(0)}...\rho^{(3)}$ and $z^{(1)}...z^{(3)}$ via (5.8), (5.10) becomes

$$\begin{aligned} \int_{-\frac{1}{2}}^{+\frac{1}{2}} \rho\frac{\partial z}{\partial \xi}\mathrm{d}\xi &= \frac{\rho_{+\frac{1}{2}} + \rho_{-\frac{1}{2}}}{2}\left(z_{+\frac{1}{2}} - z_{-\frac{1}{2}}\right) \\ -\frac{1}{10}&\left\{\left(d_{+\frac{1}{2}} - d_{-\frac{1}{2}}\right)\left[z_{+\frac{1}{2}} - z_{-\frac{1}{2}} - \frac{dz_{+\frac{1}{2}} + dz_{-\frac{1}{2}}}{12}\right]\right. \\ &\quad \left. - \left(dz_{+\frac{1}{2}} - dz_{-\frac{1}{2}}\right)\left[\rho_{+\frac{1}{2}} - \rho_{-\frac{1}{2}} - \frac{d_{+\frac{1}{2}} + d_{-\frac{1}{2}}}{12}\right]\right\}\,, \end{aligned} \tag{5.11}$$

in their respective locations), analytically differentiating, and substituting $z = z_k$. Since

$$\left.\frac{\partial\rho}{\partial z}\right|_{z=z_k} = \frac{\partial\rho/\partial s|_{s=s_k}}{\partial z/\partial s|_{s=s_k}}, \tag{5.25}$$

(5.16) leads to

$$\left.\frac{\partial\rho}{\partial z}\right|_{z=z_k} = \frac{(\rho_{k+1}-\rho_k)+(\rho_k-\rho_{k-1})}{\Delta z_{k+\frac{1}{2}}+\Delta z_{k-\frac{1}{2}}}, \tag{5.26}$$

which is only first-order accurate because it evaluates the derivative at the location $(z_{k+1}+z_{k-1})/2$ rather than the desired z_k. Similarly, (5.25) in conjunction with (5.18) leads to

$$\left.\frac{\partial\rho}{\partial z}\right|_{z=z_k} = \frac{\Delta\rho_{k+\frac{1}{2}}\Delta\rho_{k-\frac{1}{2}}\left(\Delta z_{k+\frac{1}{2}}+\Delta z_{k-\frac{1}{2}}\right)}{\left(\Delta\rho_{k+\frac{1}{2}}+\Delta\rho_{k-\frac{1}{2}}\right)\Delta z_{k+\frac{1}{2}}\Delta z_{k-\frac{1}{2}}}, \tag{5.27}$$

where $\Delta z_{k+\frac{1}{2}}$ and $\Delta\rho_{k+\frac{1}{2}} = \rho_{k+1}-\rho_k$ are elementary differences of z and ρ respectively. For the purpose of analysis of (5.27) we assume that field $\rho = \rho(z)$ is locally represented as the sum of linear background and small perturbation,

$$\rho(z) = \alpha z + \rho'(z), \tag{5.28}$$

and prove that under such conditions (5.27) agrees with (5.24) within second-order accuracy.

Substitution of (5.28) into (5.24) yields

$$\left.\frac{\partial\rho}{\partial z}\right|_{z=z_k} = \alpha + \frac{\Delta z_{k-\frac{1}{2}}\partial\rho'_{k+\frac{1}{2}}+\Delta z_{k+\frac{1}{2}}\partial\rho'_{k-\frac{1}{2}}}{\Delta z_{k-\frac{1}{2}}+\Delta z_{k+\frac{1}{2}}}, \tag{5.29}$$

where we have introduced

$$\partial\rho'_{k+\frac{1}{2}} = \frac{\Delta\rho'_{k+\frac{1}{2}}}{\Delta z_{k+\frac{1}{2}}} = \frac{\rho'_{k+1}-\rho'_k}{\Delta z_{k+\frac{1}{2}}}. \tag{5.30}$$

Substitution of (5.28) into (5.27) yields

$$\left.\frac{\partial\rho}{\partial z}\right|_{z=z_k} = \left\{\alpha + \frac{\Delta z_{k+\frac{1}{2}}\Delta\rho'_{k-\frac{1}{2}}+\Delta z_{k-\frac{1}{2}}\Delta\rho'_{k+\frac{1}{2}}}{\Delta z_{k+\frac{1}{2}}\Delta z_{k-\frac{1}{2}}} + \frac{\Delta\rho'_{k+\frac{1}{2}}\Delta\rho'_{k-\frac{1}{2}}}{\alpha\Delta z_{k+\frac{1}{2}}\Delta z_{k-\frac{1}{2}}}\right\} \Bigg/ \left[1+\frac{\Delta\rho'_{k+\frac{1}{2}}+\Delta\rho'_{k-\frac{1}{2}}}{\alpha\left(\Delta z_{k+\frac{1}{2}}+\Delta z_{k-\frac{1}{2}}\right)}\right], \tag{5.31}$$

so far without any approximation. Now we assume that the second term in square brackets is much smaller than the preceding 1 and apply a Taylor expansion,

$$\frac{1}{1+x} = 1 - x + x^2 - \dots, \tag{5.32}$$

retaining only linear terms with respect to $\Delta\rho'$:

$$\begin{aligned}\left.\frac{\partial\rho}{\partial z}\right|_{z=z_k} &= \alpha + \frac{\Delta z_{k+\frac{1}{2}}\Delta\rho'_{k-\frac{1}{2}}+\Delta z_{k-\frac{1}{2}}\Delta\rho'_{k+\frac{1}{2}}}{\Delta z_{k+\frac{1}{2}}\Delta z_{k-\frac{1}{2}}} \\ &\quad - \frac{\Delta\rho'_{k+\frac{1}{2}}+\Delta\rho'_{k-\frac{1}{2}}}{\Delta z_{k+\frac{1}{2}}+\Delta z_{k-\frac{1}{2}}} + \mathcal{O}\left(\left(\frac{\Delta\rho'}{\alpha\Delta z}\right)^2\right) \\ &= \alpha + \partial\rho'_{k-\frac{1}{2}} + \partial\rho'_{k+\frac{1}{2}} \\ &\quad - \frac{\partial\rho'_{k+\frac{1}{2}}\Delta z_{k+\frac{1}{2}}+\partial\rho'_{k-\frac{1}{2}}\Delta z_{k-\frac{1}{2}}}{\Delta z_{k+\frac{1}{2}}+\Delta z_{k-\frac{1}{2}}} + \mathcal{O}\left(\left(\frac{\partial\rho'}{\alpha}\right)^2\right),\end{aligned} \tag{5.33}$$

which then can be easily transformed into (5.29). In its turn, this verifies that harmonic averaging of elementary differences (5.18) results in second-order accurate evaluation of the first derivative on a nonuniform grid as long as the approximated function is smooth in the sense that change of its first derivative within two consecutive unequal grid intervals is small relative to the derivative itself.

Cubic spline (5.15), algebraic (5.16), and harmonic (5.18) averaging require boundary conditions for the interpolated fields, since their respective formulas cannot be applied near the boundaries directly. These boundary conditions arise from the need to use an extended stencil (in comparison with basic second-order schemes) and are essentially artificial; this is a common problem for high-order discretizations. In principle, these boundary conditions can be avoided by shortening the stencil near the boundary, which is equivalent to lowering the order of accuracy there. Lateral boundaries present somewhat lesser difficulty since one often applies Neumann (no-normal-gradient) conditions to the elementary differences $\rho_{i+1,j,k}-\rho_{i,j,k}$ on the coast line, which are typically implemented via an appropriate masking rules for a coast line of arbitrary shape. These boundary conditions are physically justifiable even in a stratified case, if it is implied that the corresponding differences $z_{i+1,j,k}-z_{i,j,k}$ also vanish, hence differencing of ρ is horizontal, and no-normal-gradient is physically consistent with no-flux lateral boundary conditions for heat and salt. Vertical boundaries are more difficult to treat, especially near the bottom, because grid resolution is often coarse, and physically justifiable conditions are elusive. In this case an extrapolation rule must be used near the boundary.

- Neumann: $\partial f/\partial s = 0$ at locations corresponding to $s_{N+\frac{1}{2}}$ and $s_{\frac{1}{2}}$, i.e., on the physical boundaries of the domain, which are at half-intervals outside f_N and f_1, respectively,

$$d_N = \frac{6}{5}(f_N - f_{N-1}) - \frac{7}{15}d_{N-1} \tag{5.34}$$

$$d_1 = \frac{6}{5}(f_2 - f_1) - \frac{7}{15}d_2. \tag{5.35}$$

• Compute $d_{i,k}$ and $dz_{i,k}$, which are harmonic averages of $\Delta\rho_{i,k\pm\frac{1}{2}}$ and $\Delta z_{i,k\pm\frac{1}{2}}$ respectively, using (5.18) for all $k = 2, \ldots, N-1$.

• Apply boundary conditions at top and bottom to d and dz using an appropriate extrapolation rule, say (5.36)–(5.37). (Once computation d and dz is complete, provisional variables $\Delta\rho$ and Δz are no longer needed and may be discarded).

• At the upper half of top-most grid box, compute and store in a provisional array,

$$FX_{i,N+\frac{1}{2}} = \left[\rho_{i,N} + \frac{1}{2}(\zeta_i - z_{i,N})\frac{\rho_{i,N}-\rho_{i,N-1}}{z_{i,N}-z_{i,N-1}}\right] \times (\zeta_i - z_{i,N})$$

(derived from the assumption of a linear profile for ρ within the upper half of the top-most grid box), after which compute and store

$$FX_{i,k+\frac{1}{2}} = \int_{(\xi,s)_{i,k}}^{(\xi,s)_{i,k+1}} \rho\frac{\partial z}{\partial s}\mathrm{d}s = \frac{\rho_{i,k+1}+\rho_{i,k}}{2}(z_{i,k+1}-z_{i,k})$$
$$-\frac{1}{10}\left\{(d_{i,k+1}-d_{i,k})\left[z_{i,k+1}-z_{i,k}-\frac{dz_{i,k+1}+dz_{i,k}}{12}\right] - (dz_{i,k+1}-dz_{i,k})\left[\rho_{i,k+1}-\rho_{i,k}-\frac{d_{i,k+1}+d_{i,k}}{12}\right]\right\}$$

for $k = 1, \ldots, N-1$. (Once all FXs are computed, d and dz may be discarded).

• Compute and store elementary differences along σ-coordinates, $\Delta'\rho_{i+\frac{1}{2},k} = \rho_{i+1,k} - \rho_{i,k}$ and $\Delta' z_{i+\frac{1}{2},k} = z_{i+1,k} - z_{i,k}$. Apply masking rules to them similar to rules for horizontal velocity components;

• Compute $d'_{i,k}$ and $dz'_{i,k}$, which are harmonic averages of $\Delta\rho_{i\pm\frac{1}{2},k}$ and $\Delta z_{i\pm\frac{1}{2},k}$ respectively using (5.18). (Once this step is performed, discard $\Delta'\rho$ and $\Delta' z$.)

• Compute and store

$$FC_{i+\frac{1}{2},k} = \int_{(\xi,s)_{i,k}}^{(\xi,s)_{i+1,k}} \rho\frac{\partial z}{\partial \xi}\mathrm{d}\xi = \frac{\rho_{i+1,k}+\rho_{i,k}}{2}(z_{i+1,k}-z_{i,k})$$
$$-\frac{1}{10}\left\{\left(d'_{i+1,k}-d'_{i,k}\right)\left[z_{i+1,k}-z_{i,k}-\frac{dz'_{i+1,k}+dz'_{i,k}}{12}\right] - \left(dz'_{i+1,k}-dz'_{i,k}\right)\left[\rho_{i+1,k}-\rho_{i,k}-\frac{d'_{i+1,k}+d'_{i,k}}{12}\right]\right\}$$

for all $k = 1, \ldots, N$.

• Finally, assuming that $FC_{i+\frac{1}{2},N+1} \equiv 0$, compute

$$-\mathcal{AJ}_{i+\frac{1}{2},k+\frac{1}{2}} = FX_{i,k+\frac{1}{2}} + FC_{i+\frac{1}{2},k+1} - FX_{i+1,k+\frac{1}{2}} - FC_{i+\frac{1}{2},k},$$

and perform its vertical integration

$$-\Delta x\left[\left.\frac{\partial P}{\partial x}\right|_z\right]_{i+\frac{1}{2},k} = -g\sum_{k'}^{N}\mathcal{AJ}_{i+\frac{1}{2},k'+\frac{1}{2}}\,, \qquad (5.39)$$

for all $k = N, N-1, \ldots, 1$ (starting from top and proceeding downward), after which all FXs and FCs may be discarded. (Since sums in (5.39) for different k can be computed recursively, there is no need to store $\mathcal{AJ}_{i+\frac{1}{2},k+\frac{1}{2}}$ in a temporary array.)

Sigma-coordinate Primitive Form

As with the second-order Jacobian, this algorithm can be algebraically transformed into a σ-Coordinate primitive form which resembles (1.1). This implies that the $P_{i,k}$ field is computed first at all $\rho_{i,k}$ points by means of vertical integration[9],

$$P_{i,N} = g\left[\rho_{i,N} + \frac{1}{2}(\zeta_i - z_{i,N})\frac{\rho_{i,N}-\rho_{i,N-1}}{z_{i,N}-z_{i,N-1}}\right] \times (\zeta_i - z_{i,N})\,,$$

and

$$P_{i,k} = P_{i,k+1} + g\frac{\rho_{i,k+1}+\rho_{i,k}}{2}(z_{i,k+1}-z_{i,k})$$
$$-\frac{g}{10}\left\{(d_{i,k+1}-d_{i,k})\left[z_{i,k+1}-z_{i,k}-\frac{dz_{i,k+1}+dz_{i,k}}{12}\right] - (dz_{i,k+1}-dz_{i,k})\left[\rho_{i,k+1}-\rho_{i,k}-\frac{d_{i,k+1}+d_{i,k}}{12}\right]\right\}$$

for all $k = N-1, \ldots, 1$ going downward, after which

$$-\Delta x\left[\left.\frac{\partial P}{\partial x}\right|_z\right]_{i+\frac{1}{2},k} = P_{i,k} - P_{i+1,k} - g\cdot FC_{i+\frac{1}{2},k}\,, \qquad (5.40)$$

where $FC_{i+\frac{1}{2},k}$ is computed the same way as in the previous section.

Note that $FC_{i+\frac{1}{2},k}$ has obvious similarity with the second term in the r.h.s. of (1.6), and within second-order accuracy it is interpreted simply as the product of ρ and local slope of σ-coordinate. The more accurate fourth-order scheme (5.40) computes $FC_{i+\frac{1}{2},k}$ as the integral of the last term in (1.6) along the lower facet of curvilinear trapezoidal element shown as the shaded area in Fig. 7. Although it produces a result algebraically identical to the

[9]This algorithm is known as `prsgrd32A.F` in the ROMS code

algorithm described in the previous section, the present form offers some technical advantages by eliminating the need to store $FC_{i+\frac{1}{2},k}$ in provisional arrays, since no differencing of FCs is present in (5.40). This results in a more compact code overall.

6. Further Seamount Tests

Fig. 9 shows time histories of all six error measures defined above in a format similar to Fig. 5. Among the previously tested schemes we retain for comparison are the original $\gamma = 0$ (labeled as POM), the optimal density-Jacobian with $\gamma = 0.5$, and the Lin, 1997, finite-volume method. We include two versions of our proposed schemes, one using harmonic averaging of elementary slopes (labeled *Cubic H* on Fig. 9) and one using algebraic averaging (labeled *Cubic A*). At coarse resolution *Cubic H* shows the lowest error by all measures with a substantial edge. At the same time, *Cubic A* and $\gamma = 0.5$ results are comparable, consistent with the previous experience that straightforward attempts to increase the order of accuracy of the scheme do not produce any actual gain in accuracy under realistic simulation conditions like those in the present test problem. Note that the vertical grid spacing on Fig. 4 reaches $1200m$ near the bottom, which exceeds the e-folding scale of $500m$ for the initial $\rho(z)$ in (4.7); similarly, in places with extreme values of $r_x = 2.4$, the vertical distance between consecutive grid points along σ-coordinate lines may reach $800m$. In both cases the consecutive differences of ρ in (5.16) may be different by more than a factor of three, which unavoidably causes oscillation of cubic interpolant and a corresponding increase of error of the PGF scheme. In contrast to *Cubic A*, harmonic slope averaging (5.18) used by *Cubic H* effectively suppresses oscillations, resulting in smallest error on the coarse grid.

In comparison with $\gamma = 0$ and $\gamma = 0.5$, *Cubic H* and *Cubic A* produce somewhat smaller error in the barotropic mode relative to total kinetic energy (cf., panels $\mathcal{E}_{\rm bar}/\mathcal{E}_{\rm kin}$ and $\langle V\rangle_{\rm max}$, especially in the fine resolution case where $\mathcal{E}_{\rm bar}/\mathcal{E}_{\rm kin}$ falls below 40%). This is encouraging because erroneous barotropic flow does not have tendency to decrease due to advective compensation mechanism (Mellor *et al*, 1998), which makes it potentially more dangerous type of error in comparison with the baroclinic one.

Our results for improved PGF accuracy invite comparisons with the previously published ones (Beckmann & Haidvogel, 1993,1997; McCalpin, 1994; Chu & Fan, 1997, 1998; Mellor *et al*, 1998; Song, 1998). Doing so, however, is difficult because despite the similarity of the problem set up, crucial differences remain, and we find that the results are highly sensitive to values and forms of viscous operators used, topographic roughness parameters r_D (4.6), differences in vertical grid stretching resulting in different extreme values of r_x (2.10), many of which are not reported in the original papers. Producing such a comprehensive comparison is beyond the scope of this study, and we just restrict ourselves here to demonstrating the sensitivity of the velocity error to the value of the horizontal viscosity; see Fig 10, where in all cases we use the *Cubic H* PGF scheme. As expected, increase of horizontal viscosity results in the decrease of erroneous velocity amplitude; however most of the sensitivity occurs at early times, where the error can be easily reduced by an order of magnitude by choosing viscosity well within the range of that is reported in the literature cited above. Long-term error exhibits a somewhat weaker sensitivity, and increasing viscosity does not decrease the error as much as at early times. We believe that this is partly attributable to the form of discretized viscous operator, which itself can produces spurious currents. (In all computations presented here we used a lateral viscous operator in form of symmetric stress tensor, Shchepetkin & O'Brien, 1996, which is also similar to that of POM, but not of Beckmann & Haidvogel, 1993,1997, and McCalpin, 1994.)

In all cases the levels of energy are at least one order of magnitude higher than that of geostrophically balanced flow caused by the hydrostatic error produced by initial ρ field, which supports a primarily dynamic cause for the errors shown in Figs. 5 and 9.

7. Effect of Seawater Compressibility

Most previously known PGF schemes, including standard and weighted Jacobians, *Lin 97*, etc, are linear algorithms in the sense that an additive change to a given set of density values $\{\rho_k\}$ causes an additive change in the reconstructed profile $\mathcal{P}\left[\rho_k\right]$ and the pressure gradient,

$$\frac{\partial \mathcal{P}}{\partial x}\left[\rho^{(1)}_{i,j,k}+\rho^{(2)}_{i,j,k}\right] = \frac{\partial \mathcal{P}}{\partial x}\left[\rho^{(1)}_{i,j,k}\right] + \frac{\partial \mathcal{P}}{\partial x}\left[\rho^{(2)}_{i,j,k}\right] , \quad (7.1)$$

where $\left\{\rho^{(1)}_{i,j,k}\right\}$ and $\left\{\rho^{(2)}_{i,j,k}\right\}$ are two arbitrary sets of grid-box values. This property is a basis for the common practice in σ-modeling of subtracting a predefined background stratification from *in situ* ρ in order to reduce PGF errors. However, the property (7.1) is no longer valid for algorithms which use monotonicity constraints, such as (5.18), and, as we will see, adding or subtracting an arbitrary background ρ profile may significantly degrade the accuracy of computation of PGF. Nonlinear monotonicity constraints usually detect and prevent situations where the derivatives of the reconstructed interpolants

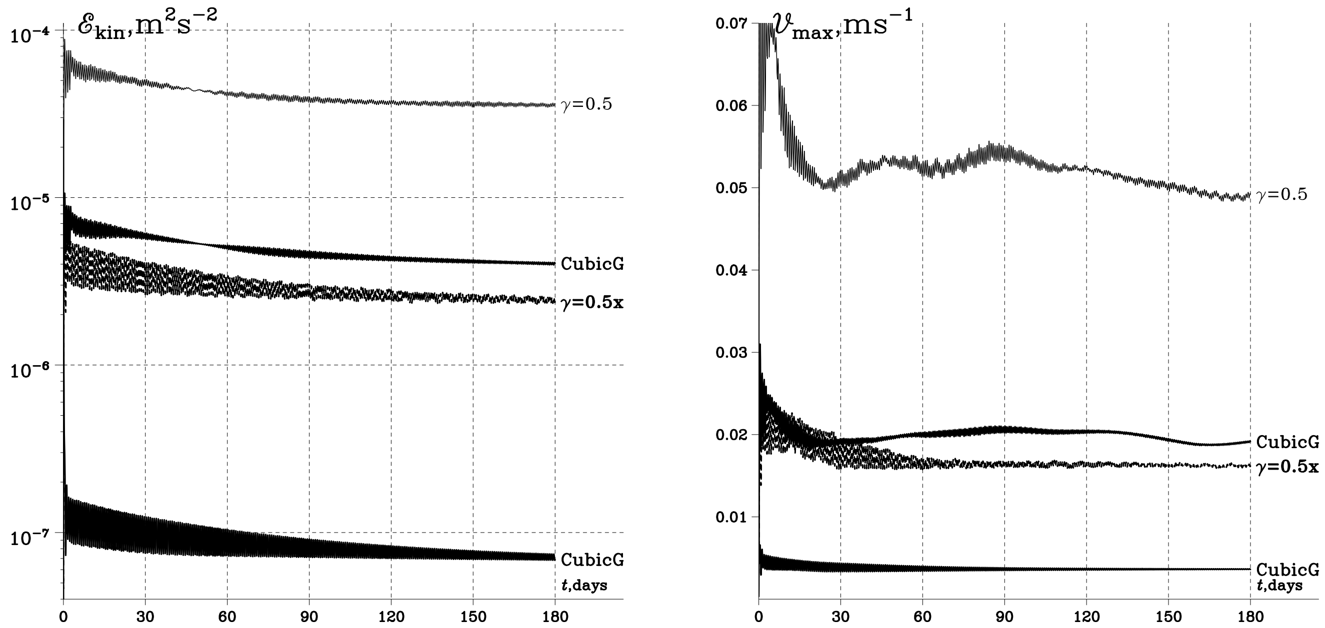

Figure 11. Time history of kinetic energy $\mathcal{E}_{\rm kin}$ and maximum velocity error $V_{\max}$ for Seamount test problem with uniform temperature and salinity ($\theta = 4^0C$ and $S = 33\,^0/_{00}$) using full, nonlinear compressible EOS (7.9) . Two upper curves labeled *Cubic H* and $\gamma = 0.5$ correspond to the resolution of $48 \times 48 \times 11$, grid points, while two lower curves are for the doubled resolution of $96 \times 96 \times 22$.

where ρ_0 and K_0 are the leading-order, constant terms in the original polynomial fits for $\rho_1(\theta, S)$ and $K(\theta, S, z)$. Since $\rho'_1(\theta, S, z) \ll \rho_0 = 999.84\ kg/m^3$ and $K'(\theta, S, z) \ll K_0 = 190925\ m$, as well as $z \ll K_0$ for any reasonable depth within the range of 0-11000 m, one can expand (7.10) in a Taylor series,

$$\rho = \rho_0 \left[1 - \frac{z}{K_0} + \left(\frac{z}{K_0}\right)^2 + ... \right] + \\ + \rho'_1 \left[1 - \frac{z}{K_0} + ... \right] + \qquad (7.11) \\ + \frac{\rho_0 K'}{K_0} \left[\frac{z}{K_0} + \frac{(K'+z)^2}{K_0^2} + ... \right] .$$

The first term on the second line is the usual baroclinic ρ perturbation, while the first term on the third line is the leading-order contribution to PGF due to the joint effect of compressibility and baroclinicity (commonly known as thermobaricity). All terms on the first line depend on z only, and, therefore, they should not contribute to PGF; however, as we will demonstrate, they turn out to be a major source of PGF error in σ models. In principle, both second-order Jacobian and our new scheme produce zero error, if density is a linear function of z (such as the leading term on the first line of (7.11)), but the remaining terms are nonlinear and their polynomial fits are not exact, resulting in nonzero PGF error.

To illustrate the severity of the problem we set up a Seamount test problem in which temperature and salinity are set to be uniform, $\theta = 4^0C$ and $S = 33\,^0/_{00}$, and ρ is computed using the full EOS (7.9); thus, ρ is a function of z only and varies only due to compressibility. The results are shown on Fig. 11, in a format similar to Fig. 5. The overall level of errors is comparable with that on Figs. 5–9 for similar algorithms and resolutions, with some qualitative differences in spatial distributions and temporal behavior of this new type of error, resulting in a maximum erroneous velocity of 2 and 5 cm/s for coarse-resolution implementations of the $\gamma = 0.5$ and Cubic H schemes, respectively. This indicates that the inclusion of compressibility in the straightforward way most likely causes more inaccuracy in the velocity field due to σ-coordinate PGF errors than the inaccuracy caused by unphysically neglecting compressibility effects altogether (i.e., using just $\rho_1(\theta, S)$ instead of $\rho(\theta, S, z)$ from (7.9) for the purpose of PGF computation). The problem is further aggravated by the fact that there is no advective compensation mechanism, cf., Mellor *et al*, 1994, for this kind of error, resulting in an erroneous velocity field determined purely from geostrophic balance with hydrostatic PGF error generated by nonlinear terms on the first line of (7.11). If the Coriolis frequency is set to zero (as on the Equator), there is nothing to balance the erroneous PGF and the model becomes unstable. Unlike the case of Fig. 5, now we do not observe any significant sensitivity

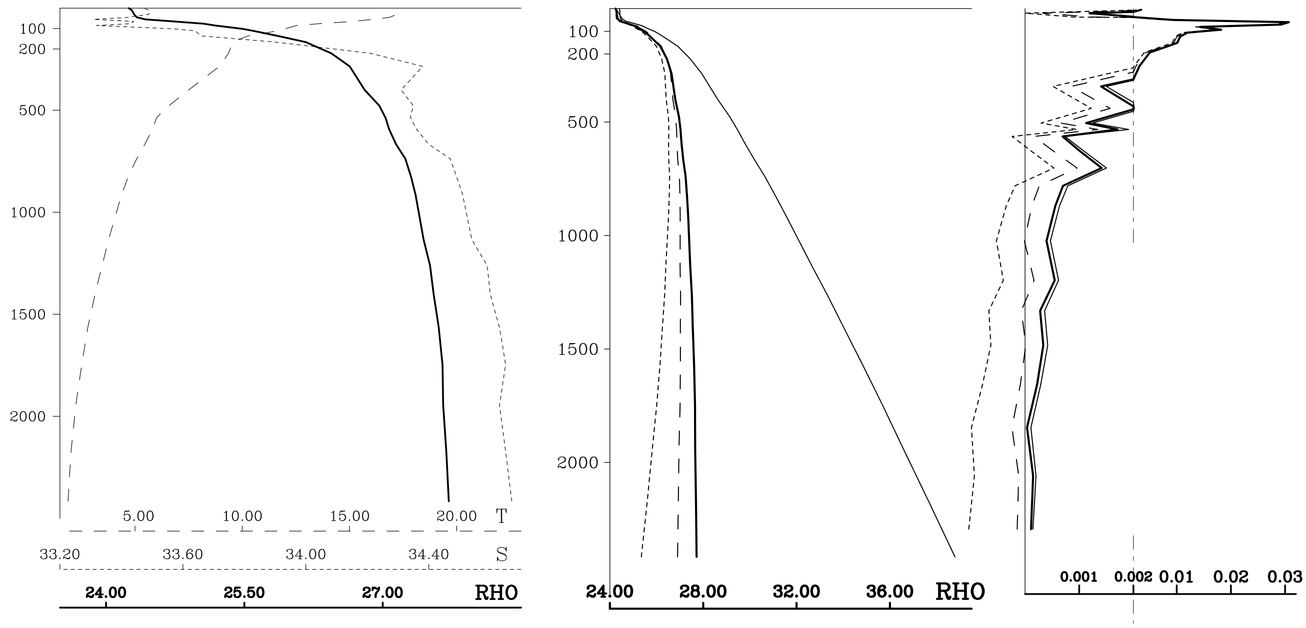

Figure 12. Left – An example of typical measured profiles of *in situ* temperature, salinity, and potential density (with the effect of compressibility removed and $\rho_0 = 1000$ subtracted). These profiles are measured within CalCOFI domain off the California coast. Courtesy of John Moisan. **Middle** – Effect of compressibility in different versions of EOS: *thick solid line* – ρ_1 – density with effects of compressibility removed (this is the same profile on the left); *thin solid line* – ρ – density *in situ* using full nonlinear EOS (7.9); *dotted line* – simplified EOS (7.12)with linearized compressibility effect; *dashed line* – dynamically relevant density $\rho - \rho_{\rm bak}$ defined by (7.14). **Right** – Vertical derivatives of the corresponding profiles in the middle computed using simple finite differences for all cases, except for *in situ* density ρ (thin solid line), where adiabatic differencing (7.7)is used instead. Note stepped horizontal scale.

$(i+1, k+1$ and $i, k)$ directions. This is evident from the fact that all terms in curly brackets in (5.11) already depend only on such differences, and any combination of the preceding terms—the second-order fluxes (2.12)—can be rewritten into the diagonal Jacobian (2.5), which contains only simple diagonal differences but no midpoint averages. Then (7.16) can be discretized by replacing elementary ρ differences with adiabatic differences,

$$\begin{aligned} d^{(\rm ad)}_{i,k+\frac{1}{2}} &= \left[\rho_{i,k+1} - \rho_{i,k}\right]\big|_{\rm ad} \\ &= -\frac{\alpha_{i,k+1} + \alpha_{i,k}}{2}\left[\theta_{i,k+1} - \theta_{i,k}\right] \\ &\quad + \frac{\beta_{i,k+1} + \beta_{i,k}}{2}\left[S_{i,k+1} - S_{i,k}\right] , \end{aligned} \tag{7.19}$$

which are harmonically averaged in a manner of (5.18), hence enforcing the non-oscillatory property of the cubic interpolant (5.11) and maintaining the sign of the stratification.

The algorithm just described by-passes computation of ρ completely at the expense of the need to compute two fields, α and β as functions of θ, S, and z. Although it does not involve any approximation to EOS, the passive compressibility terms, cf., (7.11), are "differentiated out" at the stage of replacing $\rho_{\rm in\,situ}$ with α and β. The computational cost is still very high, in part because of extra work the modified PGF algorithm due to replacement of elementary ρ differences with adiabatic ones via (7.19), and, more significantly, in the EOS part, where the cost is doubled because both α and β are approximately as expensive as $\rho_{\rm in\,situ}$. Therefore, we seek practical simplifications that efficiently capture the dynamical effects of compressible EOS. We first note that (7.10) can be approximated by an expansion (cf., Sun, 1999),

$$\rho\left(\theta, S, z\right) = \rho'_1\left(\theta, S\right) + \sum_{n=1}^{n_{\max}} q_n\left(\theta, S\right)\cdot z^n , \tag{7.20}$$

with, in principle, an arbitrary accuracy, depending on the value of $n_{\max}$, and (7.12) can be viewed as the simplest truncation with $n_{\max} = 1$. A detailed assessment of the accuracy of this truncation relevant to the PGF computation—i.e., the ability to produce accurate α and β—is given in Appendix B. We furthermore note that for each n taken separately,

$$\begin{aligned} \mathcal{J}\left(q_n z^n, z\right) &= \frac{\partial}{\partial \xi}\left(q_n z^n\right)\frac{\partial z}{\partial s} - \frac{\partial z}{\partial \xi}\frac{\partial}{\partial s}\left(q_n z^n\right) \\ &= \frac{\partial q_n}{\partial \xi} z^n \frac{\partial z}{\partial s} - z^n \frac{\partial z}{\partial \xi}\frac{\partial q_n}{\partial s} = z^n \cdot \mathcal{J}\left(q_n, z\right) , \end{aligned} \tag{7.21}$$

changes the monotonicity constraint (5.20) into

$$
\begin{array}{l}
d_{i,k}^{(0)} \le d_{i,k} \le d_{i,k}^{(0)} + 2\delta \\
\text{or} \\
d_{i,k}^{(0)} \le d_{i,k} \le d_{i,k}^{(0)} - 2\delta \\
\text{or} \\
d_{i,k}^{(0)} \ge d_{i,k} \ge d_{i,k}^{(0)} + 2\delta \\
\text{or} \\
d_{i,k}^{(0)} \ge d_{i,k} \ge d_{i,k}^{(0)} - 2\delta
\end{array}
\tag{7.27}
$$

where $d_{i,k}$ is the *in situ* ρ derivative, $d_{i,k}^{(0)} \equiv {q_1}_{i,k}\partial z/\partial s$,

$$\delta = \text{minmod}\left(d_{i,k-\frac{1}{2}} - d_{i,k}^{(0)}\,,\, d_{i,k+\frac{1}{2}} - d_{i,k}^{(0)}\right)$$

and the function *minmod* is equal to the smallest of its arguments by absolute value, if all of them have the same sign, or zero, if the signs are different.

The new compressible EOS PGF scheme differs from the original Cubic H scheme only in the procedure of computing ρ derivatives via harmonic averaging of adiabatic differences (7.26), while all subsequent steps in the algorithm remain the same. This method has the following properties:

- PGF error due to compressibility of seawater with uniform θ and S has been eliminated completely, regardless of particular choice of reference values ρ_0, K_0, etc. Hence, it is not necessary to repeat the experiment of Fig. 11 using the new approach;
- Unlike $\rho(\theta, S, z)$, both $\rho_1'(\theta, S)$ and $q_1(\theta, S)$, do not explicitly depend on z which allows us to split the derivative of *in situ* ρ into adiabatic and compressible parts. Hence, a straightforward application of harmonic averaging (5.18) to the adiabatic term guarantees positive stratification along the interpolated profile as long as the discrete values are positively stratified.
- The computational cost of this new PGF scheme and the associated EOS does not exceed significantly the cost of the original Cubic H scheme and EOS.

8. Realistic Tests for the Atlantic Ocean

In order to illustrate the practical effects of the new PGF scheme and alternative treatment of compressibility, we include results from several realistic Atlantic Ocean simulations. The model bathymetry shown on Fig. 13 is the same as in Haidvogel *et al*, 2000, with 3/4 degree spatial resolution and S-coordinate stretching parameters

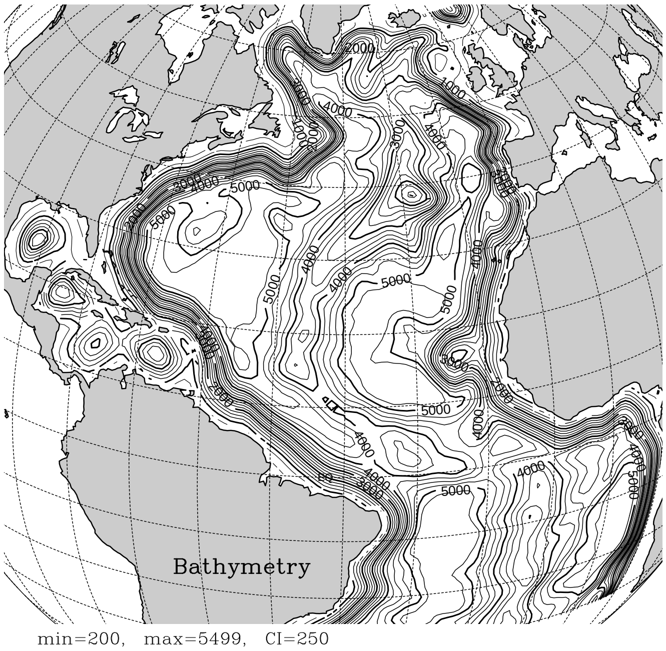

Figure 13. Model Bathymetry for a 3/4 degree-resolution Atlantic Ocean simulation

$\vartheta = 5$, $\vartheta_b = 0.4$, and $h_{\min} = 200$m, which translate into a maximum topographic "r-factor" of 0.195 and a maximum σ-grid stiffness ratio of $r_x = 3.82$. Hence, despite its relatively smooth appearance, this model topography causes a strong violation of the hydrostatic consistency criterion and a relatively large change of bottom depth per horizontal grid interval compared to common σ-modeling practices. The test results reported here may be also considered as verification of robustness of the newly designed algorithm with respect to coarse vertical resolution and a non-smooth ρ field, which has been recognized as a major concern for PGF schemes with higher than second-order accuracy, Kliem & Pietrzak, 1999.

For the flat-stratification test problem, the wind stress and surface heat and fresh-water fluxes are set to zero, and we choose a horizontally uniform potential temperature profile (in ^0C),

$$\theta = 0.2 + 6\exp\{-|z|/2500\} + 20\exp\{-|z|/250\} \tag{8.1}$$

and a uniform salinity $S = 35^0/_{00}$. The amplitude and e-folding scales for this profile are representative of an instantaneous profile in a selected location in the tropical Atlantic (where, as we will see, the largest PGF errors occur), rather than basin-scale averaged profile. We believe that this is more appropriate, since PGF errors are controlled by local profiles, while a horizontally averaged profile tends to be much smoother. (For a similar test, Mellor *et al*, 1994, chose an e-folding scale of 1000 m, which is also comparable with horizontally averaged profiles re-

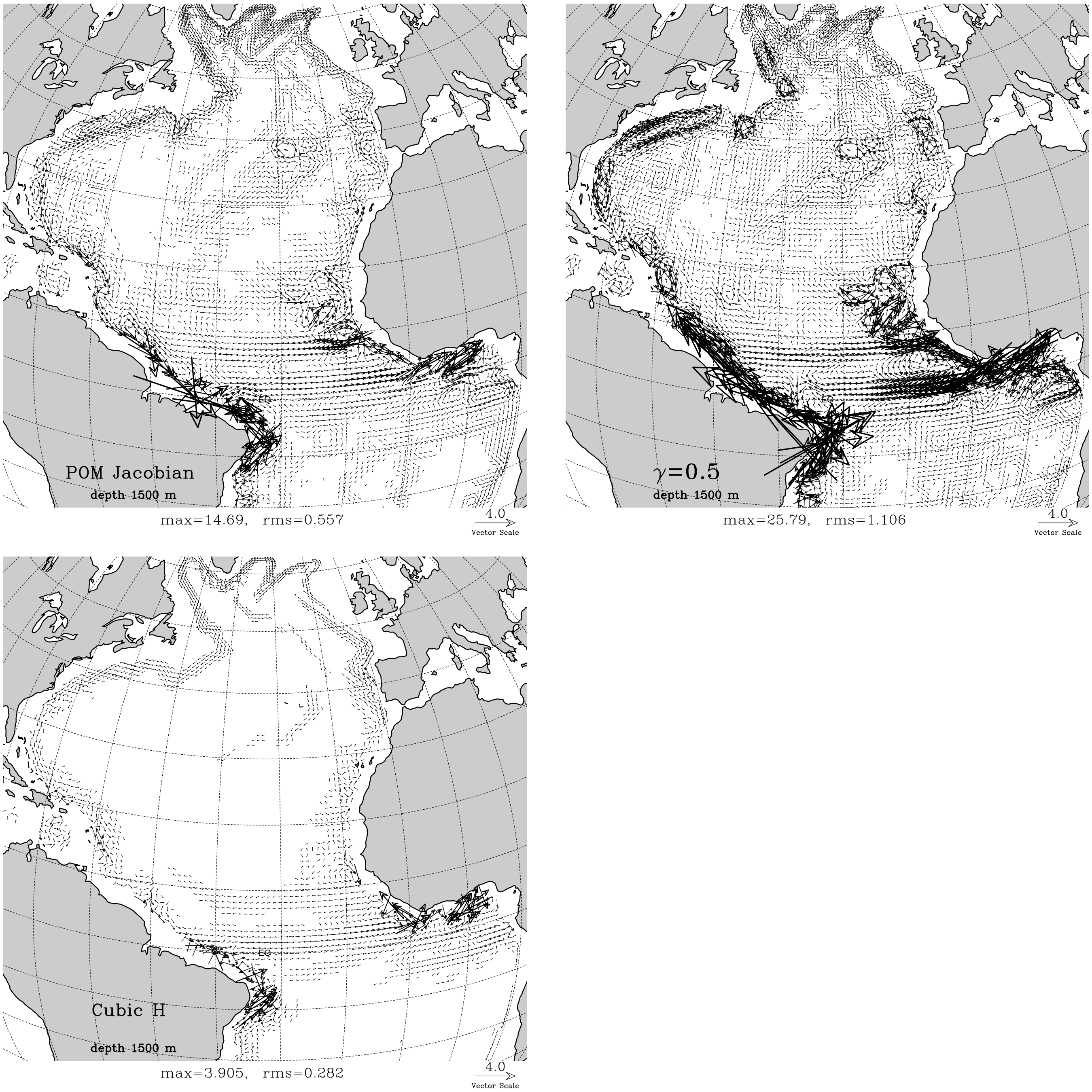

Figure 15. Spurious currents from a flat-stratification, pressure-gradient error test problem for a realistic bathymetry Atlantic Ocean model configuration after 60 days of simulations, starting from rest initial condition. In all three cases shown here, EOS compressibility effects were turned OFF completely by setting $\rho_{\mathrm{in\,situ}}(\theta, S, z) = \rho_1(\theta, S)$; Velocity scale is in cm/sec; vectors with magnitude smaller that 0.05 cm/s are not shown. **Top-left** – POM Jacobian ($\gamma = 0$); **Top-right** – $\gamma = 0.5$-scheme; Note that for $\gamma = 0$ and 0.5 flow directions are opposite near Brazilian coast, where the largest errors occur. **Lower-left** – *Cubic H* pressure-gradient algorithm.

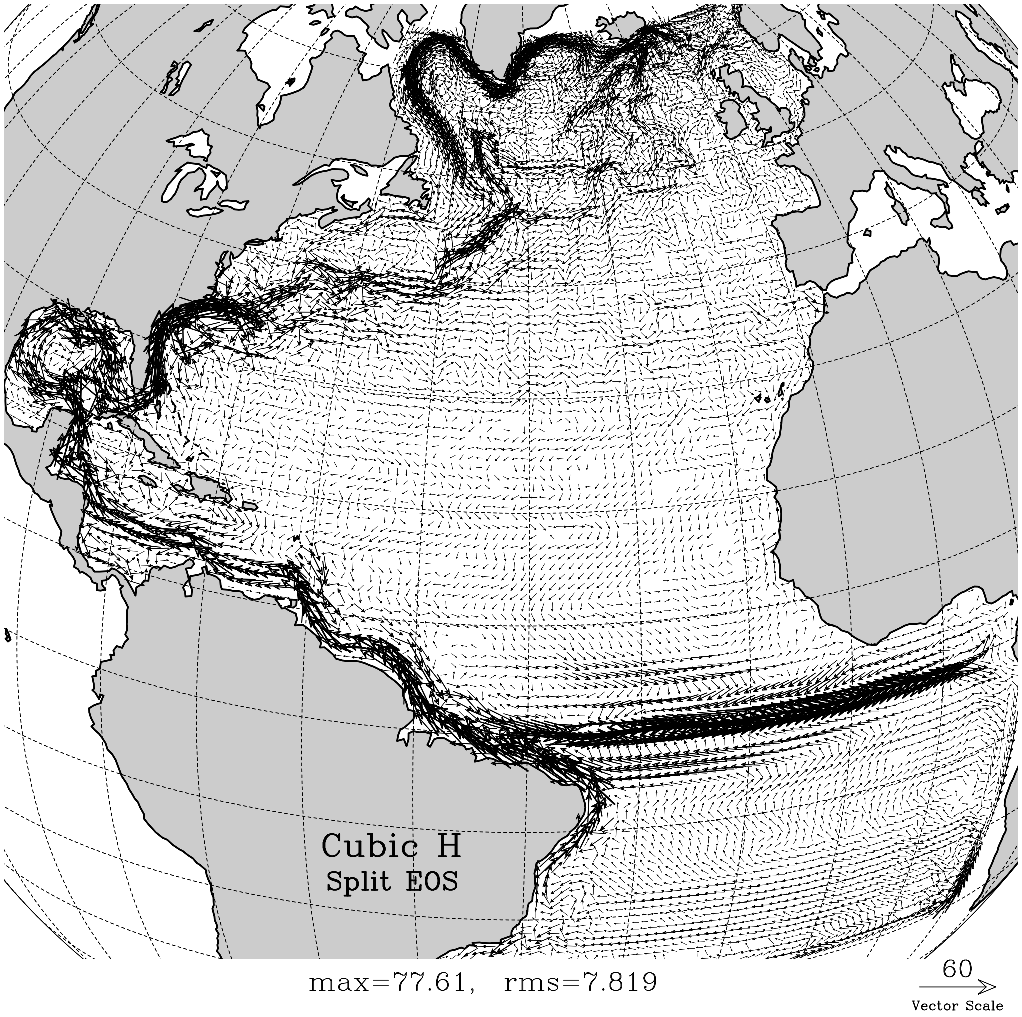

Figure 17. Near-surface currents time-averaged over 6-month period after 3-year spin up of North-Atlantic model simulation starting from Levitus climatological initial conditions and running under realistic wind and thermodynamic forcing, using modified *Cubic H* + (7.26) pressure-gradient algorithm and split EOS (7.20) with $n_{\max} = 1$ (same combination as on lower-left panel of Fig. 16).

be balanced only by Coriolis or viscous forces. Subtraction of the dominant part of the mean passive compressibility term, $\rho_0/\left(1-|z|/K_{00}\right)$, reduces the error to some extent, but it fails to produce any significant benefit in the Equatorial region (Fig. 16, top right). On the other hand, splitting EOS into an incompressible part and a term proportional to depth (7.20) and computing derivatives of ρ via harmonic averaging of adiabatic differences (7.26) avoids any noticeable increase of error associated with compressibility (Fig. 16, lower left).

One might suggest that this reduction of error, in comparison with a straightforward computation of PGF using *in situ* ρ, is explained mainly by the effective linearization of compressibility effects in the first-order truncation of (7.20) with $n_{\max} = 1$. To explore this possibility, we made an alternative calculation in which we used the same EOS, $\rho = \rho_1(\theta, S) + q_(\theta, S) \cdot z$ (cf., (7.20) with $n_{\max} = 1$), but now the ρ_1 and $q_1 z$ terms were combined into *in situ* ρ, which is then used in the original Cubic H scheme. The result is shown in Fig. 16, lower right. Although the level of error there is slightly smaller than when using full nonlinear EOS (cf., Fig. 15, lower right), it is closer to it than t is to the results with the split or incompressible EOS (i.e., Fig. 16, lower left, or Fig. 15, lower left). Since the two compressible algorithms here differ only in the computation of ρ derivatives—specifically the choice of the reference gradient considered "neutral" by the monotonicity-enforcement algorithm, (7.27) vs. (5.20)—this indicates

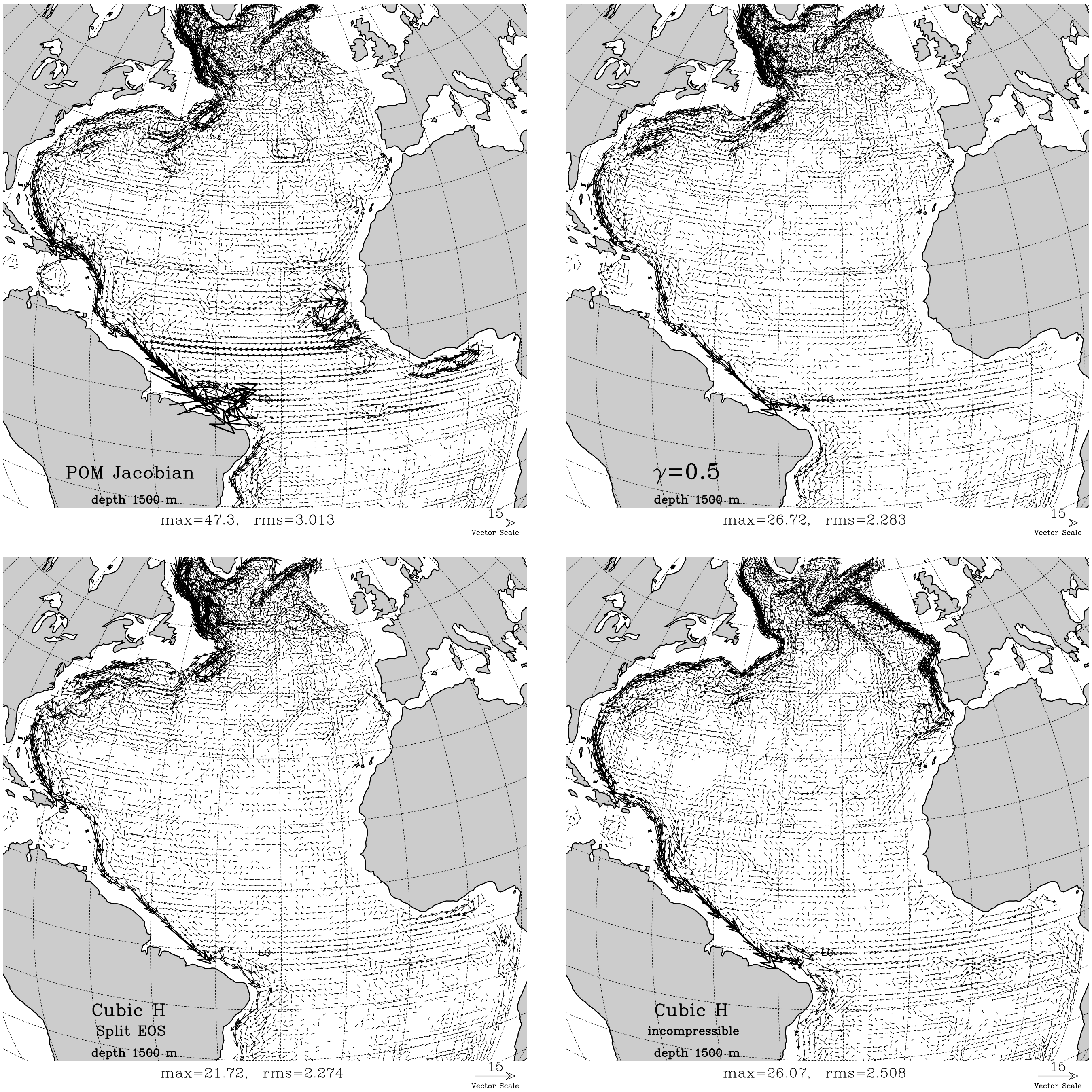

Figure 18. Same as in Fig. 17 , but at depth 1500 m, instead of near-surface, and for four different pressure-gradient algorithms: **top-left** – POM Jacobian ($\gamma = 0$), EOS by (7.14) ; **top-right** – $\gamma = 0.5$, same EOS as on top-left. Note the difference in amplitude of Deep Western Boundary Current (DWBC) off coast of Brazil; **lower-left** – modified *Cubic H*+(7.26) in combination with EOS (7.20) ; **lower-right** – *Cubic H*, compressibility terms turned OFF. Note spurious northward current off coast of Portugal, which continues toward north-west along the topographic slope. This current is due to model response to θ, S of Mediterranean outflow, and is caused by wrong temperature expansion and saline contraction coefficients because of neglect of thermobaric effect. This current is completely absent in the other three solutions. Also note artificially intensified and narrower DWBC in comparison with lower-left panel.

some features that seem likely to be spurious.

Our experience also shows that the straightforward inclusion of compressibility in *in situ* ρ calculations for PGF causes a significant increase of hydrostatic PGF error compared to EOS without compressibility. This error results in spurious currents that are the largest near the Equator, due to the diminished Coriolis frequency there. On the other hand, disregarding compressibility completely (motivated by the desire to reduce PGF error) causes significant errors in realistic simulations due to physically wrong responses of the model to temperature and salinity forcing. Our new method for splitting the compressibility terms allows us to obtain physically correct responses without increase of hydrostatic error.

9. Summary

Although PGF errors can be eliminated completely only if isosurfaces of the vertical coordinate are aligned with either geopotential surfaces or isopycnals, these two choices of the vertical coordinate have difficulties in accurately representing the top and bottom boundary conditions. This leaves σ-models as preferred, if accurate topographic and shallow-water, free-surface effects are the highest priority. Therefore, the goal of minimizing PGF errors in σ-models remains important for oceanic modeling.

An analysis of one the more successful PGF schemes to date, the second-order Jacobian, shows that, in addition to approximating the desired terms of the continuous equations with second-order accuracy, it also has important symmetries and can be written in several alternative but equivalent forms. The latter lead to different versions of high-order accuracy generalizations, depending of which form is chosen as the prototype. We find the pseudo-flux form particularly attractive. This gives the possibility of rewriting the Jacobian in the form of a contour integral, and we propose a fourth-order accurate method based on this form. In doing so we preserve the property of the original scheme that treats ρ and z as functions of transformed coordinates in a symmetric, mutually interchangeable way. Our new approach is based on reconstruction of ρ and z as continuous and continuously differentiable polynomial functions of transformed coordinates with subsequent analytical integration. Similarly to its prototype, our new method can be equivalently transformed between Density-Jacobian and σ-coordinate primitive forms. We analyze the causes of previous experience of non-robustness and limited applicability of high-order schemes designed in the past, and we pay special attention to the prevention of the appearance of spurious oscillations of polynomial interpolants in the cases where ρ can no longer be treated as a smooth field on the grid. We also develop special measures to avoid loss of accuracy associated with the use of spatially nonuniform grids that are commonly used in oceanic modeling.

Historically σ-coordinate PGF errors have been attributed mainly to hydrostatic cancellation errors. Thus, the primary focus of many previously proposed schemes has been to address this particular problem while much less attention has been paid to derived conservation properties of the discretized PGF. Our experience shows that it is not entirely the right perspective because as the model's ρ field evolves the actual magnitude of spurious velocities may become very much larger than that determined from geostrophic balance with the erroneous PGF associated with a horizontally uniform initial $\rho(z)$ field. Specifically we observe significant growth of erroneous barotropic flow in a manner previously described as "a σ error of the second kind" (Mellor *et al*, 1998).

Realistic oceanic modeling requires taking into account the compressibility of seawater. Accurate representation of this effect is especially difficult in σ-models, because the straightforward inclusion of compressibility into the EOS causes a large, dynamically passive, background vertical profile of *in situ* ρ associated with compressibility of seawater with uniform temperature and salinity. Although in theory this background profile should not generate any PGF, it is shown to be a major source of PGF error in models due to the combination of the usual numerical noncancellation in the absence of compressibility (σ-error) and the largeness of this passive compressibility effect compared to the stable stratification, particularly in the abyss where vertical resolution is typically very coarse. Furthermore, this background compressibility interferes with non-oscillatory interpolation algorithms because physically neutral stratification is no longer equivalent to the absence of a vertical gradient in ρ. To address these difficulties, we have devised a new treatment of compressibility effects that splits ρ into terms evaluated at atmospheric surface pressure and terms with compressibility, in order to isolate the latter from adding to the PGF error as it does when total ρ is used in the calculation. The new EOS formulation is shown to be sufficiently accurate, compared to the standard EOS formulation, for reliable usage in oceanic models.

Acknowledgements This study was supported by grants N00014-98-1-0165 and N00014-00-1-0249 from the Office of Naval Research. All computations presented here were performed in National Center for Supercomputing Applications (NCSA) sponsored by National Science Foundation.

restrict ourselves to the case of zero free-surface disturbance, despite the fact that (A.1) does not explicitly contain the free-surface term $PX_{i+\frac{1}{2},\zeta}$, as it occurs in (2.6)–(2.7) from SW98. Below in (A.21)–(A.23) we also show that the free-surface contribution can be naturally cast in flux-difference form of (A.1).

Multiplication of (A.1) by $u_{i+\frac{1}{2},k}$ and summation over all indices i yields,

$$\begin{aligned}\sum_{i=1}^{L-1} \widetilde{\Delta H}^{x}_{i+\frac{1}{2},k} u_{i+\frac{1}{2},k} PX_{i+\frac{1}{2},k} &= \sum_{i=1}^{L-1} \widetilde{\Delta H}^{x}_{i+\frac{1}{2},k} u_{i+\frac{1}{2},k} \left\{ -\delta_x \left(\sum_{k'=k}^{N} FX_{k'+\frac{1}{2}} \right)_{i+\frac{1}{2}} - FCX_{i+\frac{1}{2},k} \right\} \\ &= \sum_{i=1}^{L} \left\{ \delta_x \left(\widetilde{\Delta H}^{x}_{k} u_k \right)\Big|_i \left(\sum_{k'=k}^{N} FX_{i,k'+\frac{1}{2}} \right) \right\} - \sum_{i=1}^{L-1} \widetilde{\Delta H}^{x}_{i+\frac{1}{2},k} u_{i+\frac{1}{2},k} FCX_{i+\frac{1}{2},k}\,,\end{aligned} \tag{A.4}$$

where in order to obtain the second line from the first we have applied summation by parts in a manner similar to the transition from Eq. (2.22) to (2.23) in SW98, where we assume no-flux boundary conditions $u_{\frac{1}{2}} = u_{L+\frac{1}{2}} = 0$, so that the index range in the leftmost sum in the second line can be extended as necessary to include side velocity points (it should be noted that the expressions inside the leftmost sum and its inner sum in the second line are now placed at density point $\rho_{i,k}$ on horizontally staggered C-grid).

After similar manipulation with PY-terms, we derive the contribution of PGF into net kinetic energy tendency,

$$\begin{aligned}\frac{dKE}{dt}\Big|_{PGF} &= \sum_{k=1}^{N}\sum_{j=1}^{M}\sum_{i=1}^{L-1} \widetilde{\Delta H}^{x}_{i+\frac{1}{2},j,k} u_{i+\frac{1}{2},j,k} PX_{i+\frac{1}{2},j,k} + \sum_{k=1}^{N}\sum_{j=1}^{M-1}\sum_{i=1}^{L} \widetilde{\Delta H}^{y}_{i,j+\frac{1}{2},k} v_{i,j+\frac{1}{2},k} PY_{i,j+\frac{1}{2},k} \\ &= \sum_{i=1}^{L}\sum_{j=1}^{M}\sum_{k=1}^{N} \left\{ \left[\delta_x \left(\widetilde{\Delta H}^{x}_{k} u_k \right) + \delta_y \left(\widetilde{\Delta H}^{y}_{k} v_k \right) \right]\Big|_i \left(\sum_{k'=k}^{N} FX_{i,k'+\frac{1}{2}} \right) \right\} \\ &- \sum_{i=1}^{L-1}\sum_{j=1}^{M}\sum_{k=1}^{N} \widetilde{\Delta H}^{x}_{i+\frac{1}{2},j,k} u_{i+\frac{1}{2},j,k} FCX_{i+\frac{1}{2},j,k} - \sum_{i=1}^{L}\sum_{j=1}^{M-1}\sum_{k=1}^{N} + \widetilde{\Delta H}^{y}_{i,j+\frac{1}{2},k} v_{i,j+\frac{1}{2},k} FCY_{i,j+\frac{1}{2},k}\,.\end{aligned} \tag{A.5}$$

Applying discrete continuity equation

$$\frac{\partial}{\partial t} \Delta H_{i,j,k} + \delta_x \left(\widetilde{\Delta H}^{x}_{k} u_k \right) + \delta_y \left(\widetilde{\Delta H}^{y}_{k} v_k \right) + \delta_s \omega = 0, \tag{A.6}$$

where $\Delta H_{i,j,k}$ and levels $z_{k+\frac{1}{2}}$ follow evolution of free surface,

$$\frac{\partial z_{k+\frac{1}{2}}}{\partial t} = \frac{h + z_{k+\frac{1}{2}}}{h+\zeta} \cdot \frac{\partial \zeta}{\partial t} \qquad k = 1, \ldots, N\,, \qquad z_{\frac{1}{2}} \equiv -h\,, \quad \text{and} \quad z_{N+\frac{1}{2}} \equiv \zeta\,, \tag{A.7}$$

(hence (A.6) should be understood as the definition of vertical velocities $\omega_{i,j,k+\frac{1}{2}}$ as the mass fluxes across *moving* grid-box interfaces $z_{i,j,k+\frac{1}{2}}$), the first term in the r.h.s. of (A.5) may be further rewritten as

$$\begin{aligned}\sum_{k=1}^{N} \left\{ \left(-\frac{\partial}{\partial t} \Delta H_{i,j,k} - \delta_s \omega \right) \left(\sum_{k'=k}^{N} FX_{i,j,k'+\frac{1}{2}} \right) \right\} &= - \sum_{k=1}^{N-1} \left\{ \left(\frac{\partial z_{i,j,k+\frac{1}{2}}}{\partial t} + \omega_{i,j,k+\frac{1}{2}} \right) \left(\sum_{k'=k}^{N} FX_{i,j,k'+\frac{1}{2}} \right. \right. \\ - \left. \left. \sum_{k'=k+1}^{N} FX_{i,j,k'+\frac{1}{2}} \right) \right\} - \frac{\partial z_{i,j,N+\frac{1}{2}}}{\partial t} FX_{i,j,N+\frac{1}{2}} &= - \sum_{k=1}^{N-1} \omega_{i,j,k+\frac{1}{2}} FX_{i,j,k+\frac{1}{2}} - \sum_{k=1}^{N} \frac{\partial z_{i,j,k+\frac{1}{2}}}{\partial t} FX_{i,j,k+\frac{1}{2}}\,.\end{aligned} \tag{A.8}$$

To derive this we have used top and bottom kinematic boundary conditions $\omega_{N+\frac{1}{2}} = \omega_{\frac{1}{2}} = 0$, and $\partial z_{\frac{1}{2}}/\partial t = 0$ [note that $\partial z_{N+\frac{1}{2}}/\partial t \equiv \partial\zeta/\partial t \neq 0$ due to evolving free surface].

The discretized density equation is

$$\frac{\partial}{\partial t} \left(\Delta H_{i,j,k} \rho_{i,j,k} \right) = -\delta_x \left(\widehat{\rho}^{x} \cdot \widetilde{\Delta H}^{x}_{k} u_k \right) - \delta_y \left(\widehat{\rho}^{y} \cdot \widetilde{\Delta H}^{y}_{k} v_k \right) - \delta_s \left(\widehat{\rho}^{s} \cdot \omega \right)\,, \tag{A.9}$$

PGF and advection. This fundamental limitation stems from the second-order accurate definition of potential energy,

$$PE = \iiint \rho z \, \mathrm{d}x \, \mathrm{d}y \, \mathrm{d}z \approx \sum_{i,j,k} \rho_{i,j,k} \Delta H_{i,j,k} z_{i,j,k} \,. \tag{A.16}$$

- Violation of the pseudo-flux form in the uppermost grid element, common practice of subtracting background profile $\rho = \rho_{\mathrm{bak}}(z)$ from density field before computing PGF (motivated by the desire to reduce hydrostatic errors in PGF) as well as the use of nonlinear (realistic) equation of state of seawater destroy energetic consistency, cf., Gerdes, 1993.
- Since both sums (A.14) are at least second-order discrete approximations to the same continuous integral,

$$\int_{-h}^{\zeta} \rho \frac{\partial z}{\partial t} \mathrm{d}z \tag{A.17}$$

this equation already holds within the order of accuracy. Assuming[17] that $z_{i,j,k} = \frac{1}{2}\left(z_{i,j,k+\frac{1}{2}} + z_{i,j,k-\frac{1}{2}}\right)$, the second sum in (A.14) may be rewritten as

$$\sum_{k=1}^{N} \Delta H_k \rho_k \frac{\partial z_k}{\partial t} = \sum_{k=1}^{N-1} \frac{\rho_k \Delta H_k + \rho_{k+1} \Delta H_{k+1}}{2} \cdot \frac{\partial z_{k+\frac{1}{2}}}{\partial t} + \frac{1}{2} \rho_N \Delta H_N \frac{\partial z_N}{\partial t} \,, \tag{A.18}$$

which suggests

$$FX_{k+\frac{1}{2}} = \frac{\rho_k \Delta H_k + \rho_{k+1} \Delta H_{k+1}}{2} \,, \quad k = 1, ..., N-1, \quad \text{and} \quad FX_{N+\frac{1}{2}} = \frac{\rho_N \Delta H_N}{2} \tag{A.19}$$

to achieve exact cancellation in (A.14). Unless vertical grid spacing is uniform, this choice is different from $FX_{k+\frac{1}{2}} = (\rho_k + \rho_{k+1})(\Delta H_k + \Delta H_{k+1})/4$ used in the original second-order scheme. This discrepancy comes from the fact that definition of discrete potential energy (A.11) corresponds to the assumption of a piecewise-constant distribution of ρ within each vertical grid box ΔH_k, while second-order Jacobian assumes linear profiles between each pair of z_k and z_{k+1}.

Eq. (A.13) does not restrict the algorithm for computation of $FX_{i,j,N+\frac{1}{2}}$ at the uppermost grid point. We therefore propose the following method:

$$\rho^{(\mathrm{surf})} = \rho_N + \frac{\rho_N - \rho_{N-1}}{z_N - z_{N-1}} \left(z_{N+\frac{1}{2}} - z_N\right) \,, \tag{A.20}$$

where $z_{N+\frac{1}{2}} \equiv \zeta$ corresponds to free surface, after which

$$FX_{N+\frac{1}{2}} = \frac{\rho^{(\mathrm{surf})} + \rho_N}{2} \left(z_{N+\frac{1}{2}} - z_N\right) \,, \tag{A.21}$$

and

$$PX_{i,N} = \widetilde{\Delta H}^{x}_{i+\frac{1}{2},N} \left(FX_{i,N+\frac{1}{2}} - FX_{i+1,N+\frac{1}{2}} - FXC_{i+\frac{1}{2},N}\right) \,, \tag{A.22}$$

which repairs the inaccuracy of the original scheme at the top-most grid level (e.g., PGF now vanishes identically everywhere if ρ is a linear function of z). Eq. (A.22) already contains the contribution due to PGF due to free-surface disturbance: e.g., assuming that $FXC_{i+\frac{1}{2},N} = \frac{1}{2}(\rho_{i,N} + \rho_{i+1,N})(z_{i+1,N} - z_{i,N})$ and setting $\rho_i^{(\mathrm{surf})} = \rho_{i+1}^{(\mathrm{surf})} = \rho_{i,N} = \rho_{i+1,N} = \rho_0$ results in

$$PX_{i,N} = \widetilde{\Delta H}^{x}_{i+\frac{1}{2},N} \rho_0 \left(z_{i,N+\frac{1}{2}} - z_{i+1,N+\frac{1}{2}}\right) = \widetilde{\Delta H}^{x}_{i+\frac{1}{2},N} \rho_0 \left(\zeta_i - \zeta_{i+1}\right) \,. \tag{A.23}$$

[17] This choice corresponds to the finite-volume interpretation of non-uniform vertical grid, where $z_{i,j,k\pm\frac{1}{2}}$ are coordinates of grid-boxs interfaces, while $z_{i,j,k}$ are grid-box averaged z.

which has a form appropriate for computation of PGF, cf., (7.20). As follows from (7.15)–(7.17), for accurate computation of horizontal ρ and PGF, it is sufficient that EOS produces correct estimate for temperature-expansion α and saline-contraction β coefficients, while *in situ* ρ is irrelevant for this purpose. Therefore, to assess possible errors associated with the use of (B.4), we compare the α and β it produces with the original coefficients produced by the EOS from JM95.

Properties of the original EOS from JM95 are illustrated in Fig. 19, where $\rho_{\text{in situ}}$, α, and β are plotted as function of potential temperature θ and salinity S at four different depths $z = 0$. There is overall increase of $\rho_{\text{in situ}}$ with depth z, and in addition to that, there is change in slope of isopycnals with depth on the left column in Fig. 19, which is primary due to the thermobaric effect. There is a local maximum of freshwater ρ at $\theta = 4^0C$, $z = 0$, which shifts to smaller temperature and eventually disappears with increase of P (depth). Middle column shows a significant dependency of α on depth; e.g., for $\theta = 5^0C$ and $S = 33^0/_{00}$, α changes from 0.1 to 0.25 when z goes from 0 to 6000 m. β is more uniform in θ, S-space, with the exception of the limit of low salinity, and it has a relatively weak dependency on depth. As follows from Fig. 19, disregarding the thermobaric effect completely, hence using just $\rho_1'(\theta, S)$ for computation of PGF, results in an underestimate of the ρ gradient in the abyss by as much as 60%. Therefore, one needs to retain terms linear and perhaps quadratic in z in (B.4). In both approximations the resulting α and β are quite close to their values produced by EOS from JM95; so, we show only deviations of α and β from the original ones in Fig. 20. The errors are quite significant within the whole range of possible values of θ and S, especially at maximum depth z=6000m and in the limit of largest temperature and small salinity (right-bottom corner of each plot). Indeed, errors in α may be as large as 30%, while errors in β about 15%. Fortunately in realistic oceanographic conditions temperature has a tendency to decrease with depth, resulting in a much smaller range of possible values, and a similar tendency occurs in salinity field. This fact is reflected by the dashed rectangle on each plot in Fig. 20, which outlines the *domain of relevance*, meaning that nearly all realistic combinations of θ, S should occur within it, and which shrinks with depth. Within this rectangle the errors are much smaller, and, remarkably, its location coincides with the area of minimal errors. The ranges of errors in α and β for θ, S within the domain of relevance are summarized in the following table:

EOS	$\rho' + q_1 z$		$\rho' + q_1 z + q_2 z^2$	
depth	error in α	error in β	error in α	error in β
1000	-0.0026 ... -0.0008	+0.0004 ... +0.0012	-0.003 ... -0.001	+0.0004 ... 0.0012
2500	-0.0040 ... +0.0005	0.0 ... +0.003	-0.007 ... -0.003	+0.002 ... +0.001
5000	-0.008 ... +0.007	-0.008 ... -0.006	-0.005 ... -0.015	-0.004 ... 0.0

This means that, at a maximum depth of z=5000m, given characteristic values of $\alpha = 0.25$ and $\beta = 0.8$, the errors do not exceed 3% for α and 3% for β for linear truncation and slightly less for quadratic. These estimates can be viewed as the worst-case realistic scenario, and, as seen from the table above, the errors are much smaller within the upper 2500 m, which is dynamically the most active part of the ocean. Both truncations provide viable approximations for EOS and offer significant reduction of errors in comparison with neglecting compressibility completely; however, the quadratic version offers no significant improvement to justify its extra complexity .

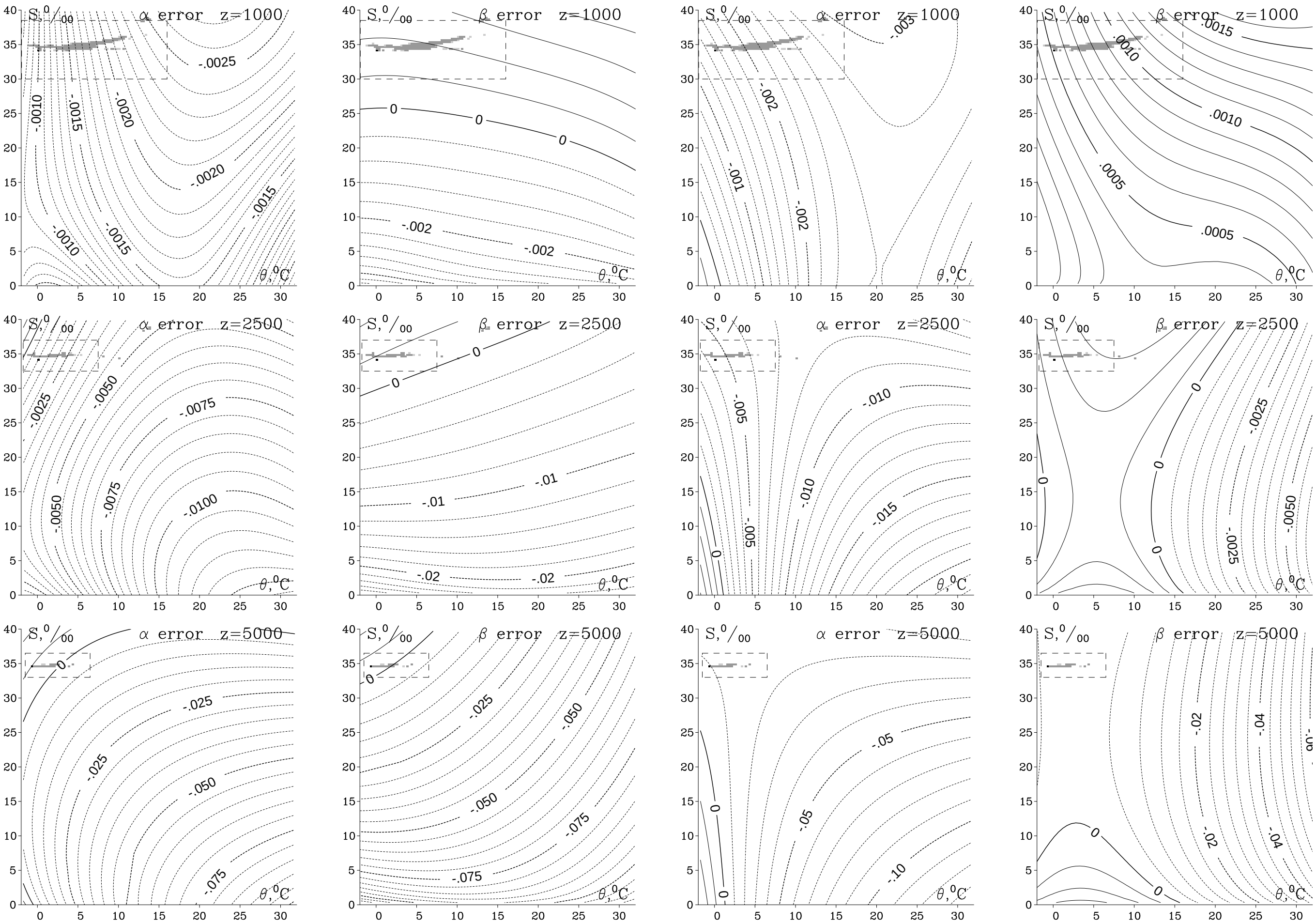

Figure 20. Errors in evaluation of thermal expansion α and salinity contaction β at three different depths, $z = 1000$, 3000, and 6000 m for linear **(left two columns)** and quadratic **(right two columns)** truncations of z-series of EOS from JM95. Errors are definded as deviations of α and β from their values computed form the original EOS (see Fig. on the previous page), which are considered as "exact" in this comparison. Dashed rectangle on each plot shows the *domain of relevance*, meaning that for realistic oceanographic conditions θ and S can occur only within this rectangle at each depth z.

Mellor, G. L., 1991: An equation of state for munerical models and estuaries. *Journ. Atmos. Oceanic Technology*, **1991**, 609-611.

Mellor, G. L., T. Ezer and L.-Y. Oey, 1994: The pressure gradient conundrum of sigma coordinate ocean models. *Journ. Atmos. Oceanic Technology*, **1994**, 1126-1134.

Mellor, G. L., L.-Y. Oey, and T. Ezer, 1998: Sigma coordinate pressure gradient errors and the seamount problem. *Journ. Atmos. Oceanic Technology*, **15**, 1122-1131.

Mesinger, F., and A. Arakawa, 1976: Numerical Methods used in atmospheric models, Vol. 1, GARP Publ. Ser. 17., World Meteor. Org., 64 pp.

Mesinger, F., 1982: On the convergence and error problems of the calculation of the pressure gradient force in sigma coordinate ocean models. *Geophys. Astrophys. Fluid Dyn.*, **19**, 105-117.

Mesinger, F. and Z. I. Janjic, 1985: Problems and numerical methods of the incorporation of mountains in atmospheric models. *Lect. Appl. Math.*, **22**, 81-120.

Michailovic, D. T., and Z. I. Janjic, 1986: Comparison of methods for reducing the error of the pressure gradient force in sigma-coordinate models. *Meteorol. Atmos. Phys.*, **35**, 177-184.

Millero, F. J., C.-T. Chen, A. Bradshaw, and K. Schleicher, 1980: A new high-pressure equation of state for seawater. *Deep-Sea Res.*, **27A**, 255-264.

Shchepetkin, A. F. and J. J. O'Brien, 1996: A Physically Consistent Formulation of Lateral Friction in Shallow Water Equation Ocean Models. *Monthly Weather Review*, **124**, 1285-1298.

Slordal, L. H., 1997: The pressure gradient force in sigma coordinate ocean models. *Int. J. of Num. Meth. in Fluids*, **24** , 987-1017.

Song, Y. T. and D. Haidvogel, 1994: A Semi-implicit ocean circullation model using a generalized topography following coordinate system, *Journ. Comp. Phys.*, **115**, 228-248.

Song, Y. T. 1998: A General Pressure Gradient Formulation for Ocean Models. Part I: Scheme Design and Diagnostic Analysis, *Monthly Weather Review*, **126**, 3213-3230

Song, Y. T. and D. G. Wright, 1998: A General Pressure Gradient Formulation for Ocean Models. Part II: Energy, Momentum and Bottom Torque Consistency, *Monthly Weather Review*, **126**, 3213-3230

Sun, S., R. Bleck, C. Rooth, J. Dukowicz, E. Cassignet, and P. Killworth, 1999: Inclusion of Thermobaricity in Isopycnic-Coordinate Ocean Models. *Journ. Phys. Ocean.*, **29**, 2719-2729.

Stelling, G. S., and J. A. Th. van Kester, 1994: On the approximation of horizontal gradients in sigma coordinates for bathymetry with steep bottom slopes. *Int. J. of Num. Meth. in Fluids*, **18** , 915-935.

Treguier, A. M., J. K. Dukowicz, and K. Bryan, 1996: Properties of nonuniform grids used in ocean general circullation ocean models. *Journ. Geophys. Res.*, **101**, 20877-20881.

Willebrand, J., B. Barnier, C. Böning, C. Dieterich, P.D. Killworth, C. LeProvost, Y. Jia, J.-M. Molines, A.L. New, 2001: Circulation characteristics in three eddy-permitting models of the North Atlantic. *Progress in Oceanography*, **48**, pp. 123-161.

This preprint was prepared with the AGU LaTeX macros v3.1. File pgf2 formatted 2003 March 26.